PLIN5 phosphorylation orchestrates mitochondria lipid droplet coupling to control hepatic lipid flux and steatosis

Sun Woo Sophie Kang[1], Lauryn A Brown[1], Colin B Miller[1], Katherine M Barrows[1,2], Jihye L Golino[1], Hanyang Liu[1], Constance M Cultraro[1], Daniel Feliciano[1], Mercedes B. Cornelius-Muwanuzi[1,5], Kirsten Remmert[2], Jonathan Hernandez[2], Andy D Tran[3], Michael Kruhlak[3], Alexei Lobanov[4], Maggie Cam[4], and Natalie Porat-Shliom[1,6]

1. Cell Biology and Imaging Sections, Thoracic and GI Malignancies Branch, Center for Cancer Research, National Cancer Institute, National Institutes of Health, Bethesda, MD, USA.
2. Surgical Oncology Program, Center for Cancer Research, National Cancer Institute, National Institutes of Health, Bethesda, MD, USA.
3. Laboratory of Cancer Biology and Genetics, Center for Cancer Research, National Cancer Institute, National Institutes of Health, Bethesda, MD, USA.
4. CCR Collaborative Bioinformatics Resource, National Cancer Institute, National Institutes of Health, Bethesda, Maryland, USA.
5. Cavendish Laboratory, Department of Physics, University of Cambridge, J. J. Thomson Avenue, Cambridge, CB3 0H3, United Kingdom.
6. Corresponding author: poratshliomn@mail.nih.gov

Abstract

Steatotic liver disease is common, yet the mechanisms by which hepatocytes cope with surges in dietary fatty acids remain unclear. Using single-cell tissue imaging (scPhenomics) and spatial proteomics, we mapped lipid handling across dietary states. Fasting remodeled mitochondria and lipid droplets (LDs), increasing mitochondria-LD contacts, whereas contacts were infrequent in Western diet-fed male mice. Fasting also elevated perilipin-5 (PLIN5), a mediator of mitochondria-LD tethering. PLIN5 overexpression modulated contact formation in a phosphorylation-dependent manner: the S155A variant enhanced organelle contacts and LD expansion, while the S155E variant reduced contacts and yielded fewer, smaller LDs. Overexpression of the S155A

variant in WD reduced lipotoxicity. These data reveal an adaptive organelle-interaction program that channels lipids during nutrient stress and is attenuated by an obesogenic diet. Our work establishes scPhenomics for spatially resolved cell-state analysis and identifies PLIN5 phosphorylation as a lever to tune hepatocyte lipid flux, suggesting therapeutic potential for targeting mitochondria-LD coupling.

Introduction

Steatotic liver disease, caused by excessive hepatic lipid buildup, is a common condition affecting about one-third of adults worldwide [1]. Interestingly, fasting also induces lipid buildup in the liver due to increased fatty acid (FA) transport from adipose tissue and a concurrent reduction in Very Low-Density Lipoprotein (VLDL) secretion [2, 3]. However, it remains unclear how hepatocytes manage this lipid influx during nutrient deprivation and whether these mechanisms can be harnessed to restore function in steatosis.

The liver plays a central role in regulating lipid metabolism, alternately promoting lipid oxidation and synthesis depending on nutrient availability. Following a meal, lipids produced by the liver are sent to adipose tissue for storage. During fasting, FAs stored in adipose tissue are mobilized to the liver, where they are used to synthesize alternative fuel sources [4]. Notably, in homeostasis, lipid metabolism is spatially segregated within the liver, with periportal hepatocytes primarily involved in lipid oxidation and pericentral hepatocytes associated with lipid synthesis [5, 6]. How these different populations of hepatocytes adapt to the influx of lipids observed during fasting and disease remains poorly understood.

Metabolic flexibility, defined as the ability to sense and respond to changes in nutrient availability, is crucial for regulating adaptive organ responses [2, 7]. In hepatocytes, this flexibility depends on the rapid structural reorganization of organelles, which form interconnected networks known as metabolic sub-compartments. For example, the remodeling of mitochondrial-LD contacts has been shown to facilitate lipid transfer either for oxidation in the mitochondria or storage in LD, depending on the cell and tissue type [8, 9]. Perilipin 5 (PLIN5) is one of several proteins known to facilitate mitochondria-LD interactions [10, 11]. It localizes to LD and recruits mitochondria via a unique C-terminal region [12-14]. While remodeling of mitochondrial and LD

organization has been shown in liver physiology and disease, its functional outcomes remain unclear, partly because of challenges in studying these processes in tissues.

In this study, we examined the effects of increased hepatic lipid flux on organelle organization, focusing on mitochondria and LDs – key organelles that form contact sites to regulate lipid metabolism [15, 16]. Using a novel single-cell phenotypic profiling (scPhenomics) approach across different nutritional states, we discovered that mitochondria-LD contact sites are upregulated throughout the lobules of fasted mice but not in mice fed a short-term WD to mimic steatotic liver disease. Combined with spatial proteomics, we identified the upregulation of PLIN5. *In vivo* overexpression of PLIN5 promoted the formation of mitochondria-LD contact sites in a phosphorylation-dependent manner and increased triglyceride (TG) storage in LDs. In short-term WD feeding, forming mitochondria-LD contacts protected hepatocytes from lipotoxicity by channeling potentially harmful free fatty acids (FFA) into LDs. Consistently, prolonged exposure to WD, in both mouse and human samples, was associated with increased abundance of mitochondrial-LD interactions. These findings suggest that the dynamic assembly and disassembly of mitochondria-LD contact sites play a pivotal role in hepatic lipid management and may offer a therapeutic target.

Results

Mitochondria and LD topologies mirror the spatial zonation of hepatic lipid utilization and synthesis.

Hepatocytes are organized along sinusoids within the lobule, the functional unit of the liver (Extended Fig. 1A). Recent studies, including our own, have demonstrated that mitochondrial morphology, LD content, and lipid metabolism vary across the periportal-pericentral axis (PP-PC) [17-19]. We mapped organelle topology at single-cell resolution to further investigate the relationship between organelle structure and lipid metabolism. To this aim, confocal images of liver sections from transgenic mtDendra2 mice [20] stained with BODIPY and phalloidin to mark mitochondria, LDs, and cell structure, respectively, were acquired (Fig. 1A). The orientation of the PP-PC axis was determined using actin labeling of the bile ducts in the portal triad (Extended Fig. 1B-D). In addition, Dendra2 fluorescent intensity was consistently

68 higher in PP regions, providing an additional indirect landmark for tissue orientation (Extended
69 Fig. 1E).

70 We extracted cellular and organelle features using a custom Python-based workflow
71 (Python v. 3.10) that employs deep-learning segmentation [21]. The segmented hepatocytes (Fig.
72 1B) were assigned a spatial coordinate (a value 0-1) by calculating their distance from the central
73 vein and dividing it by the total PP-PC length (Fig. 1C). The PP-PC axes were manually cropped
74 (dashed rectangle). Similarly, we segmented organelles and measured geometrical parameters
75 (such as area, density, sphericity; see Materials and Methods) using the region props function
76 within the scikit-image [22] and (Fig. 1D). Analysis of eighteen PP-PC axes from three mice showed
77 an average axis length of 250 microns comprising 12-16 cells per axis (Fig. 1E). To ensure there
78 was at least one hepatocyte per bin, we divided the PP-PC axes into 12 bins with bin 1 being the
79 closest to the portal vessels and bin 12, closest to the central vein. Over 80% of the cells analyzed
80 in the segmented regions were HNF4α hepatocytes (Extended Fig. 1F).

81 We plotted representative mitochondrial and LD features across the PP-PC axis
82 (Supplementary data 1). Mitochondria in portal and mid-lobular hepatocytes displayed higher
83 sphericity (where a value of 1 indicates a perfect sphere) and lower density. In contrast,
84 pericentral hepatocytes (bins 9-12) exhibited lower sphericity, indicating a more tubular
85 morphology, along with increased mitochondrial density (Fig. 1F). LDs appeared sparse and small
86 in the portal regions (bins 1-3). A lower LD abundance persisted through bin 9, followed by a sharp
87 increase in bins 10-12, reflecting the higher LD content in pericentral hepatocytes (Fig. 1G). The
88 average LD area gradually increased from bins 3-9 before slightly decreasing in pericentral
89 regions, where LD numbers were the highest (bins 10-12; Fig. 1G).

90 To validate that measurements from two-dimensional (2D) sections accurately represent
91 the three-dimensional (3D) morphology of organelles, we also assessed mitochondrial and LD
92 features in confocal Z-stacks (Extended Fig. 2). We manually segmented individual hepatocytes
93 and rendered cell and organelle surfaces using Imaris software (Extended Fig. 2A and B). The
94 inverse relationship between mitochondrial sphericity and density that we observed in 2D was
95 confirmed in 3D (Extended Fig. 2C). Similarly, LD features were also zonated along the PP-PC axis
96 in both 2D and 3D datasets (Extended Fig. 2D). Dimensionality reduction had no impact on

97 organelle features, showing similar trends in both 2D and 3D. Cell area in the 2D and 3D datasets
98 is shown (Fig. 1H and Extended Fig. 2E). An illustration summarizing the organelle features
99 observed in three independent experiments is shown (Extended Fig. 2F).

100 Next, we examined whether the combination of topological features encoded spatial
101 signatures. Principal Component Analysis (PCA) was performed by integrating the mitochondrial
102 and LD features in Supplementary data 1. The analysis showed that neighboring hepatocytes
103 cluster together (Fig. 1I). Each PCA dot represents the averaged mitochondrial and LD features for
104 each bin/cell along the PP-PC axis (R1-R12). Three clusters emerged: R1-R3, R4-R10, and R11-R12.
105 The inclusion of neighboring cells within clusters may reflect overlapping functions (Fig. 1I).

106 Overall, the single-cell phenotypic profiling (scPhenomics) of mitochondria and LDs
107 efficiently used 2D datasets, allowing faster data acquisition, larger sample sizes, and automated
108 analysis. This novel scPhenomics approach recapitulates spatial signatures associated with the
109 functional dichotomy of lipid oxidation versus synthesis/storage, potentially defining the hepatic
110 zones responsible for lipid handling.

111 **Increased lipid flux rewires organelle circuits in the zonated liver.**

112 To examine how increased hepatic lipid influx impacts organelle features, we subjected
113 mtDendra2 mice to different dietary conditions: control diet (CNTR), fasting overnight (16 hours),
114 or fed a WD for four weeks. Liver sections were stained with BODIPY and phalloidin to label LDs
115 and cell structure, respectively, followed by scPhenomics workflow analysis (Fig. 2A-C;
116 Supplementary data 1).

117 Fasting leads to hepatic lipid accumulation due to increased lipid influx from adipose
118 tissue. As expected, LD content increased across the entire lobule (Fig. 2B). While LD size
119 remained relatively uniform, the number of LDs was higher in pericentral (PC) hepatocytes.
120 Mitochondria in periportal (PP) and mid-lobular regions appeared longer and thicker (Fig. 2B,
121 insets). Notably, long and thick mitochondria frequently wrapped around LDs, forming extensive
122 contact sites between the two organelles (Fig. 2B, insets). However, a subset of mitochondria
123 within each hepatocyte retained spherical morphology and did not interact with LDs (Fig. 2B
124 arrowheads).

125 Dietary lipid influx also leads to hepatic lipid accumulation in WD-fed mice. Four weeks of
126 Western diet (WD) consumption was sufficient to induce simple steatosis (Extended Fig. 3A)
127 without causing lobular inflammation or hepatocellular ballooning (Extended Fig. 3A). To rule out
128 the possibility that de novo lipogenesis (DNL) was activated [23, 24], we examined the expression of
129 DNL enzymes and transcription factors (Extended Fig. 3C). Increased lipid influx due to fasting led
130 to transcriptional inhibition, as previously reported [24]. However, four weeks of WD feeding had
131 no effect on expression levels, suggesting that steatosis in WD-fed mice was due to esterification
132 of dietary lipids to form LDs. One exception was the expression levels of stearoyl-CoA desaturase
133 1 (SCD1) (Extended Fig. 3C). SCD1 activity is crucial for TG packaging and LD expansion [25, 26], which
134 may represent an adaptive response to lipid excess.

135 Although WD-fed mice accumulated LD throughout the lobule, their size, number, and
136 distribution differed markedly from those in fasted mice (compare Fig. 2B and C). Specifically, LDs
137 in PP and mid-lobular hepatocytes were larger than those in PC regions. The WD-fed mice had
138 more spherical mitochondria with reduced LD interactions (Fig. 2C). Overall, increased exogenous
139 lipid flux, whether through fasting or WD, triggered distinct remodeling of both LDs and
140 mitochondria. Employing scPhenomics allowed for precise quantification of organelle features
141 across different zones and dietary conditions (Fig. 2D and E). Notably, most features were
142 influenced by both the spatial positioning of the cells and the dietary intervention. This supports
143 the notion that LD and mitochondrial features encode spatial morphological signatures of
144 zonation, providing insights into the cellular metabolic state.

145 Next, we integrated topological features from mitochondria and LDs to assess how spatial
146 signatures changed in response to dietary perturbation. When plotted on a 2D PCA, hepatocytes
147 from CNTR, fasted, and WD-fed mice formed tightly packed clusters, highlighting the significant
148 impact of dietary state on organelle topology (Fig. 3A). Incorporating a third component into the
149 analysis further increased the spatial diversity within each dietary group. This demonstrates the
150 distinct remodeling of organelles that depends on both the spatial positioning of the cell and the
151 metabolic state (Fig. 3B). We used a dendrogram combined with a heatmap to further examine
152 the information encoded by organelle features. This approach uses unsupervised clustering to
153 group mitochondria and LD average features based on similarity. The resulting heatmaps reveal

154 distinct spatial patterns of organelle features under different nutritional conditions. CNTR-fed
155 hepatocytes clustered into roughly three groups, consistent with the PCA data and potentially
156 representing three zones. In contrast, fasted and WD-fed hepatocytes clustered into at least two
157 groups of neighboring cells (Fig. 3C).

158 To examine how individual cells along the PP-PC axis (R1-R12) respond to either fasting or
159 WD, Pearson's correlation coefficient was calculated, and the pairwise correlations are shown in
160 the heatmap (Fig. 3D). Compared with organelles from CNTR-fed cells, fasted organelles showed
161 low correlation coefficient values (light-dark purple), indicating that fasting induces extensive
162 remodeling of LD and mitochondria architecture. Conversely, organelle features from WD-fed
163 livers exhibited a high correlation with the corresponding features from the CNTR diet, indicating
164 low organelle remodeling in WD-fed livers. However, a subset of PP hepatocytes (R1-R3) was
165 significantly affected by WD, as demonstrated by the low coefficient values when compared with
166 CNTR.

167 Of the features we measured, mitochondria-LD contacts were significantly affected by
168 fasting and WD (Fig. 2). The distribution of mitochondria-LD contacts across the lobule and diet
169 is shown in Fig. 3E. In the CNTR diet, LD content was low and localized to PC hepatocytes (Fig.
170 1G), consistent with the absence of mitochondria-LD overlapping pixels in PP and mid-lobular
171 regions (R1-R8), and relatively low pixel overlap in PC regions. Conversely, fasting dramatically
172 increased the overlapping pixels throughout the lobule, except for R11 and R12 in PC regions. In
173 contrast, WD-fed mice exhibited only a modest increase in overlapping pixels, with values similar
174 to those measured in PC regions of CNTR-fed mice (Fig. 3E). The heightened LD-mitochondria
175 interactions in response to fasting and the significant reduction of these interactions in WD-fed
176 mice were relatively uniform across the lobule.

177 **Comparative proteomics of sorted hepatocytes from fed and fasted mice**

178 To identify candidates that mediate mitochondria-LD interactions, we performed spatial
179 proteomics. PP and PC hepatocytes were enriched from four ad-lib-fed CNTR and overnight-fasted
180 mice using surface markers and fluorescence-activated cell sorting (FACS, as previously described
181 [18]). The sorted hepatocytes and unsorted total control were subjected to tandem mass tag (TMT)-
182 based quantitative mass spectrometry for total proteome analysis. Out of 4,999 proteins

183 identified, 1,865 (37%) in CNTR-fed mice and 1,734 (35%) in fasted mice exhibited zonation
184 (Supplementary data 2). PCA analysis shows clustering of the spatially sorted hepatocytes is
185 influenced by their lobular position (PP or PC) and the diet (fed or fasted) (Extended Fig. 4A).
186 Plotting of the PC/PP ratios in CNTR-fed or fasted hepatocytes shows that sorting of hepatocytes
187 was not influenced by fasting (Extended Fig. 4B and C).

188 The fasting response in the two hepatocyte populations was examined using volcano plots
189 (Fig. 4A). A significant overlap was observed between PP and PC hepatocytes in both upregulated
190 and downregulated proteins. For example, the mitophagy receptor BNIP3, which is enriched in
191 PC regions [18, 27, 28], was upregulated in both PP and PC hepatocytes during fasting, consistent with
192 increased mitophagy under these conditions. Notably, over half of the PP and PC proteomes
193 remained unchanged in response to fasting, suggesting that zonation is largely preserved during
194 nutritional stress, with only a subset of the proteome undergoing remodeling (Extended Fig. 4D).
195 Pathway analysis revealed that many regulated pathways are common to PP and PC hepatocytes
196 and were linked to mitochondrial function and lipid metabolism (Extended Fig. 4E).

197 In ad-libitum CNTR diet-fed mice, many hepatic lipid pathways (summarized in Fig. 4B) are
198 zonated, as shown by the nonuniform expression of key enzymes (Fig. 4C). In response to fasting,
199 lipid pathway proteins were either upregulated or downregulated throughout the lobule (Fig. 4C
200 compares PP and PC in the fasted state). As expected, the expression of proteins involved in FA
201 and cholesterol synthesis was largely reduced during nutrient deprivation. An exception was
202 observed in proteins involved in TG synthesis, an anabolic process that paradoxically increases
203 during fasting [29]. This likely facilitates the temporary storage of the excess free FA in LDs to prevent
204 lipotoxicity. Additionally, proteins involved in catabolic processes, such as FA lipolysis, oxidation,
205 and ketogenesis, were also upregulated (Fig. 4C).

206 To understand how mitochondria-LD contacts form in the fasted liver, we examined the
207 expression of proteins involved in mediating these interactions. In the fed liver, PP-PC zonation
208 observed in the expression of proteins related to mitochondrial dynamics and LD formation (Fig.
209 4D and E, compare PP and PC columns in fed mice) may be related to the differences in
210 mitochondrial topology and LD content (Fig. 1F and G). For instance, proteins associated with
211 mitochondrial biogenesis were highly expressed in PP hepatocytes, consistent with our previous

212 findings of greater mitochondrial mass in PP regions [18]. In response to fasting, many of these
213 proteins were upregulated, aligning with the extensive remodeling observed using scPhenomics
214 (Figs. 2 and 3). Notably, the LD coat protein, PLIN5, was significantly upregulated in the fasted
215 liver (Fig. 4E). Indeed, basal PLIN5 levels in livers from CNTR and WD-fed mice were comparable
216 but doubled in response to fasting (Fig. 4F). Additionally, endogenous PLIN5 localized to the
217 mitochondria-LD interface in fasted mice (Extended Fig. 5A). In summary, in homeostasis (i.e.,
218 fed mice), conflicting metabolic processes are spatially separated at the protein level. However,
219 in fasting, only the essential metabolic processes are upregulated and carried out by all
220 hepatocytes.

221 To determine if mitochondria-LD interactions can be remodeled in WD-fed mice, we fasted
222 (overnight) WD-fed mice. Mitochondria-LD interactions were quantified using co-localization
223 analysis in Imaris software (Extended Fig. 5B-C). Fasting induced mitochondrial elongation and
224 enhanced mitochondria-LD interactions in both the fasted and WD-fasted mice. Notably, LD size
225 increased, with larger droplets observed in fasted WD-fed mice, suggesting that mitochondria-LD
226 contact sites may facilitate channeling lipids for storage in LDs (Extended Fig. 5B). While 4-week
227 WD feeding causes steatosis, organelle dynamics remain functional and responsive to fasting,
228 making it a valuable experimental model for manipulation.

229 **Mitochondria-LD contact sites promote LD expansion in fed mice**

230 To investigate the functional role of mitochondria-LD contact sites, we overexpressed
231 PLIN5 in the mouse liver, using an AAV8 viral vector. Age-matched mice were fed either CNTR or
232 WD for two weeks, followed by the overexpression of PLIN5 variants. Specifically, these included
233 the WT PLIN5, a truncated version lacking the mitochondria binding domain (PLIN5 CΔ (1-424)),
234 and two phosphorylation mutants: a phospho-null (PLIN5 S155A) and a phospho-mimetic (PLIN5
235 S155E). Four weeks following the viral transduction, liver tissue and serum samples were
236 collected for microscopy and biochemical analysis (Fig. 5A and Supplementary Fig. 1).

237 Next, we assessed the impact of PLIN5 overexpression on LDs and mitochondria
238 morphologies using scPhenomics. Representative images of PP, mid-lobular (M), and PC
239 hepatocytes from mice fed a CNTR diet are shown in Fig. 5B (corresponding whole lobule images
240 in Extended Fig. 6). When compared to null, the overexpression of WT PLIN5 caused only minor

241 changes in LD size without changing their overall lobular distribution. However, WT PLIN5
242 overexpression significantly affected mitochondrial morphology. Hepatocytes 1-6 showed an
243 increased circularity index (spherical morphology), whereas hepatocytes 7-12 exhibited a lower
244 circularity index (tubular; Fig. 5D comparing WT PLIN5 with the control null). Hepatocytes
245 overexpressing PLIN5 S155A displayed elongated mitochondria closely associated with large LDs
246 throughout the lobule, despite being fed the CNTR diet. In contrast, hepatocytes expressing PLIN5
247 S155E had fewer, smaller, and more sparsely distributed LDs (Fig. 5C). Mitochondria in these cells
248 were predominantly spherical, with a reduced mitochondria area (Fig. 5D). Overexpression of the
249 truncated PLIN5 CΔ (1-424) variant, which lacks the mitochondria binding domain, did not affect
250 mitochondrial morphology but led to the formation of small LDs throughout the lobule, likely due
251 to a dominant negative effect on lipolysis [30]. Lastly, when comparing the ability of PLIN5 variants
252 to promote mitochondria-LD interactions, PLIN5 S155A demonstrated the most pronounced
253 effect across the entire lobule (Fig. 5E). Together, these findings suggest that PLIN5-mediated
254 mitochondria-LD contact sites promote lipid storage in a phosphorylation-dependent manner.

255 **Mitochondria-LD contacts mitigate oxidative stress induced by 4-week feeding of WD**

256 We examined the influence of PLIN5 overexpression on mitochondria-LD interactions in
257 WD-fed mice. Representative images from PP, M, and PC hepatocytes are shown in Fig. 6A
258 (corresponding whole lobule images, Extended Fig. 7A). Overexpression of WT PLIN5 in WD-fed
259 mice noticeably affected mitochondria length, similar to that observed in the CNTR diet-fed mice.
260 However, under these conditions, mitochondria-LD contact sites appeared more frequently than
261 in CNTR diet-fed mice (Fig. 6A, comparing WT and null). In hepatocytes expressing PLIN5 S155A,
262 mitochondria-LD contacts were observed throughout the lobule. In contrast, hepatocytes
263 expressing PLIN5 S155E displayed mitochondria that were round and that rarely wrapped around
264 LDs (Fig. 6A). In addition, the LD content in tissues expressing WT PLIN5 and PLIN5 S155E was
265 lower when compared with PLIN5 S155A (Extended Fig. 7A). As expected, the truncated variant,
266 PLIN5 CΔ (1-424), failed to recruit mitochondria to LDs. Together, the phenotypes induced by
267 overexpression of PLIN5 variants in the CNTR diet were consistent with those observed in WD.
268 Furthermore, in both CNTR and WD, PLIN5 S155A and S155E variants impacted mitochondrial

269 morphology and facilitated the assembly and disassembly of mitochondria-LD contacts,
270 respectively (Fig. 6A and B).

271 Next, we examined how the overexpression of PLIN5 variants in mice fed either CNTR or
272 WD affected whole body and liver physiology. WD-fed mice gained significant weight compared
273 to those on the CNTR diet. Overexpression of PLIN5 variants had no additional effect on body
274 weight, serum cholesterol, and FFA (Extended Fig. 7B, D, and E). However, the increase in serum
275 glucose levels, caused by WD, was significantly reduced in mice expressing the PLIN5 S155E
276 variant (Extended Fig. 7C). Tissue TG levels in PLIN5 S155A-expressing mice on WD were higher
277 than those measured in null-expressing mice (Fig. 6C). This is consistent with the idea that
278 mitochondria-LD contact sites promote TG storage in LDs. Consistently, although FFA levels
279 reached saturation in WD-fed mice, the difference between CNTR-fed and WD-fed mice was
280 greater in PLIN5 S155E, supporting higher lipolysis activity (Fig. 6D). These results support the
281 hypothesis that mitochondria-LD interactions facilitate lipid storage.

282 The rise in TG levels resulted from the esterification of dietary FAs to form TG, rather than
283 activation of DNL, as expression levels of lipogenesis enzymes, at both the RNA and protein levels,
284 were unchanged, nor the phosphorylation status of key enzymes (Extended Fig. 8). However, WD
285 and the overexpression of PLIN5 variants had an additive effect on SCD1 expression, which was
286 not observed in CNTR diet-fed mice (Extended Fig. 8A). SCD1 converts saturated FAs into
287 monounsaturated FAs (MUFAs), a crucial step in the synthesis and storage of TGs within LDs.
288 Because upregulation of SCD1 was observed in PLIN5 S155A, S155E, and CΔ (1-424) variants, but
289 only S155A displayed mitochondria-LD contact, larger LDs, and higher TG levels. The MUFAs
290 produced by SCD1 may cooperate with PLIN5 S155E to upregulate oxidative genes and smaller
291 LDs, as previously shown [15, 31]. We conclude that mitochondria-LD interactions promoted the
292 incorporation of excess dietary lipids into TG and storage in LDs.

293 Excess FAs in WD cause oxidative stress and damage to membranes, leading to hepatocyte
294 injury and inflammation [32-34]. We hypothesized that mitochondria-LD interactions reduce
295 lipotoxicity by promoting the storage of excess FFA. To test this, we measured NADP/NADPH
296 levels, reduced glutathione (GSH), and Malondialdehyde (MDA). The measured values were log_2-
297 transformed and analyzed in R using the limma package. For each assay, a linear model was fit

298 with diet (CNTR vs. WD) and PLIN5 variant as factors. Two contrasts were tested: 1) Assessing
299 within-variant the influence of the WD by comparing WD samples to the mean of the CNTR diet
300 (i.e., whether the linear WD/CNTR fold change differs from 1) and 2) Assessing whether the WD
301 effect in each variant differed from that in the null group. This comparison reveals if the
302 magnitude of the PLIN5 variant WD/CNTR diet change significantly deviates from the change in
303 the null WD/CNTR diet.

304 Four weeks of WD feeding led to a significant increase in MDA, a reporter for lipid
305 peroxidation, in null control mice (Fig. 6E). Although the MDA levels were significantly higher in
306 all WD-fed, PLIN5 variants overexpressing mice, only PLIN5 S155A levels were significantly lower
307 than the null control, suggesting that mitochondria-LD contact reduce lipid peroxidation (Fig. 6E).
308 An opposite trend was measured with the redox state indicator NADP/NADPH. Four weeks of WD
309 feeding resulted in lower NADP/NADPH levels in null, WT, and S155A variants. However, the
310 S155E had significantly higher NADP/NADPH levels compared with null, indicating an oxidative,
311 potentially damaging environment (Fig. 6F). Lastly, reduced glutathione serves as an antioxidant,
312 alleviating oxidative stress. Levels of GSH were significantly lower in PLIN5 S155E, consistent with
313 a more oxidizing and potentially harmful environment (Fig. 6G). Collectively, by sequestering
314 excess FA into LDs, mitochondria-LD interactions mitigate cellular damage caused by the
315 overabundance of FFAs.

316 **Mitochondria-LD contacts are associated with higher lipid content in mice and humans**

317 To investigate whether mitochondria-LD interactions are associated with lipid buildup
318 over time, mtDentra2 mice were fed a WD for 4, 8, and 12 weeks. Liver sections were labeled,
319 imaged, and analyzed with scPhenomics. Mitochondria-LD contacts were more frequent after 12
320 weeks on WD (Extended Fig. 9A-B). Following 12 weeks of WD feeding, LD total area increased,
321 and mitochondria became tubular, indicated by lower circularity values (Extended Fig. 9C). PLIN5
322 expression, however, was unchanged (Extended Fig. 9D).

323 The association between mitochondria-LD contacts was also examined in the human liver.
324 Histopathology was performed on twelve liver biopsies from healthy donors (10 females and 2
325 males; cohort description in Materials and Methods). Steatosis in the samples is incidental, of
326 unknown origin, and reflects the prevalence of steatosis in the population. The samples were

327 divided into three groups based on lipid content (Fig. 7A-B). To examine mitochondria-LD
328 interactions, liver sections were stained to label mitochondria and LD (Fig. 7C). High-resolution z-
329 stacks of PP and PC hepatocytes were captured, and cellular and organelle surfaces were
330 rendered using Imaris software (Fig. 7D). Although no significant difference was observed in the
331 number of LD per cell (Fig. 7F), the volume distribution of LDs in the "mild" group was notably
332 higher (Fig. 7G), as was the extent of mitochondria-LD colocalization per cell (Fig. 7H). Despite the
333 limited sample size, the expression levels of PLIN5 were higher in livers with higher lipid content,
334 consistent with mitochondria-LD interactions (Fig. 7I). These findings establish a correlation
335 between lipid content and mitochondria-LD interactions, as well as their remodeling over the
336 course of chronic WD exposure.
337
338 **Discussion**
339 This study examined how increased lipid flux affects the structure, organization, and
340 function of organelles across different liver zones. We developed an imaging-based technique
341 with a single-cell resolution to interrogate organelle topology in the native tissue environment.
342 Applying scPhenomics to map changes in organelles, we identified distinct zonal patterns that
343 depend on nutritional status. To our knowledge, using organelle features as classifiers of function
344 has mainly been applied to cells in culture. This phenotypic profiling offers novel insights into liver
345 zonation and organelle interactions, highlighting their functional roles in tissue adaptation to
346 metabolic cues. Our study also highlights the utility of scPhenomics in identifying spatially
347 relevant phenotypes that can be integrated with other single-cell methods [19, 35, 36].
348 One prominent structural adaptation we identified was the remodeling of mitochondria-
349 LD contact sites in response to nutritional stress. In fasted livers, mitochondria-LD contacts
350 spanned the lobule, while in WD-fed tissues, they were scarce (Fig. 2B-C and 3E). These
351 differences link mitochondrial-LD interactions with lipid metabolism, consistent with prior studies
352 linking them with lipid oxidation or storage [37-40]. We show that mitochondria-LD contacts facilitate
353 FA esterification to form TG for storage, thereby reducing lipotoxicity by confining potentially
354 harmful FFA in LDs. This explains the high abundance of mitochondria-LD interactions in the
355 fasted liver (Fig. 2B). The absence of mitochondria-LD interactions in short-term WD-fed mice is

356 consistent with inefficient storage of FFA in LDs, which contribute to inflammation and cell
357 damage. To examine this mechanistically, we identified proteins involved in mitochondria-LD
358 interactions using spatial proteomics.

359 The LD coat protein, PLIN5, was upregulated in the fasted liver. On the surface of LDs,
360 PLIN5 inhibits lipolysis by directly binding to Adipose Triglyceride Lipase (ATGL), thus indirectly
361 promoting LD expansion [30]. During fasting, however, Protein Kinase A (PKA) phosphorylates PLIN5
362 on S155, facilitating the release of FAs via lipolysis [15, 31, 38]. We found that *in vivo* overexpression
363 of PLIN5 S155A promoted extensive mitochondrial-LD interactions, increased TG content, and
364 enlarged LD size. Conversely, mitochondria did not interact with LD in PLIN5 S155E-overexpressing
365 livers, consistent with the dissociation of PLIN5 and the utilization of FAs. Interestingly, in starved
366 myoblasts, PLIN5 phosphorylation promotes FA transport into the mitochondria for oxidation
367 rather than storage in LDs [39]. These findings suggest that PLIN5-mediated mitochondrial-LD
368 contacts direct lipid flux differently across cell types and nutritional states. We were unable to
369 measure the direction of FA transfer in the current study due to the challenges of performing this
370 assay *in vivo*. Further experiments are needed to fully elucidate the regulatory mechanisms across
371 organ systems and nutritional states.

372 Several studies have reported that fasting induces the formation of the mitochondria-LD
373 contact site [2, 3]. Interestingly, mitochondria-LD contact sites have also been reported in mice fed
374 a high-fat diet and in genetic mouse models of obesity [17, 41]. While we detected mitochondria-LD
375 contacts in fasted mice, we did not initially observe them in short-term WD-fed mice. Extending
376 WD feeding in mice was accompanied by a rise in mitochondria-LD interactions (Extended Fig. 9).
377 In the healthy human liver, higher mitochondria-LD colocalization was observed in livers with
378 higher lipid content, which was also associated with higher PLIN5 expression (Fig. 7D-H). Overall,
379 our results show that mitochondria-LD contacts are remodeled over time, consistent with the
380 progressive nature of steatotic liver disease [42, 43]

381 During short-term WD exposure, mitochondria-LD contacts protect from oxidative stress.
382 Overexpression of PLIN5 S155A reduced lipid peroxidation and improved redox imbalance, while
383 PLIN5 S155E worsens these effects (Fig. 6E-G). Increasing PLIN5 benefits lipid and glucose
384 regulation, promoting cellular health [14, 44, 45]. We propose that fasting-related lipid influx remodels

385 mitochondria-LD contacts to support storage and prevent lipotoxicity, whereas in nutrient excess,
386 this adaptive response is disrupted, leading to harmful lipid buildup. Notably, PLIN5 S155A
387 overexpression in WD-fed mice reduces damage by channeling FFA into LDs. However, prolonged
388 WD exposure may turn mitochondria-LD contacts into contributors to disease progression (Fig. 7,
389 Extended Fig. 10). Because FFA levels are not significantly reduced by PLIN5 overexpression, it is
390 plausible that PLIN5 overexpression protects against lipotoxicity via an alternative mechanism.
391 Furthermore, our study supports the notion that PLIN5-mediated contacts promote FFA
392 esterification; however, it remains inconclusive whether mitochondria attached to lipid droplets
393 contribute to DNL. Additional experiments are needed to determine whether dissociation of
394 mitochondrial-LD interactions can reverse and prevent disease progression. Supporting this is a
395 recent study showing PLIN5 deletion protects against MASLD [46]. Overall, these findings highlight
396 the critical role of dynamic contact sites in lipid management and cellular health (Fig. 8).
397 Lipid-related pathways are compartmentalized across different organelles [17, 47, 48]. Fasting
398 led to the upregulation of proteins involved in membrane contact sites, indicating enhanced
399 organelle interactions (Fig. 4E). This suggests rewiring of organelle-organelle interactions beyond
400 mitochondria and LDs [5, 38]. Notably, Mitofusin 2 (Mfn2) and Mitoguardin 2 (MIGA2), both of which
401 localize to the ER, facilitate lipid transfer between mitochondria and the ER, and subsequently
402 store lipids in LDs [49, 50]. Since the ER plays a key role in lipid metabolism and glycemic control, the
403 benefits of PLIN5 S155A overexpression in high-fat diet mice likely involve ER-mediated processes.
404 Future studies involving scPhenomics could deepen understanding of these organelle interactions
405 [37, 51, 52].
406 The study underscores the critical role of mitochondrial morphology and organelle
407 interactions in metabolic flexibility. In the fed state, mitochondrial subpopulations facilitate lipid
408 oxidation and storage in PP and PC, respectively [38, 40, 53]. Nutritional stress, such as fasting, triggers
409 a unified mitochondrial response across the liver, driven by PLIN5 modulation, enabling
410 simultaneous lipid oxidation to support ketogenesis and temporary storage in LD to avoid
411 damage. These dynamic interactions are vital for metabolic adaptation and may be disrupted in
412 chronic liver disease, influencing liver cancer development [27, 54].
413

Contact information

Natalie Porat-Shliom, Center for Cancer Research, National Cancer Institute. Building 10, Room 12C207 MSC 1919, Bethesda, MD 20892. Phone: 240-760-6847. Email: poratshliomn@mail.nih.gov.

Financial Support

This work was supported by the Intramural Research Program at the NIH, National Cancer Institute (1ZIABC011828). The contributions of the NIH authors were made as part of their official duties as NIH federal employees, are in compliance with agency policy requirements, and are considered Works of the United States Government. However, the findings and conclusions presented in this paper are those of the authors and do not necessarily reflect the views of the NIH or the U.S. Department of Health and Human Services. The authors have no conflicts to report.

Acknowledgments

We thank Dr. Sarah Cohen, UNC-Chapel Hill, for the PLIN5 constructs. We thank Drs. Sudipto Das and Thorkell Andresson from the CCR Proteomics Facility at the Frederick National Laboratory for Cancer Research. We thank Dr. David E. Kleiner, from the Laboratory of Pathology, Center for Cancer Research, NCI, for pathology evaluation of human samples (Fig. 7A). We thank Pranali Pathare Mangat of 3P Scientific Communications for scientific editing.

Figure legends

Figure 1. LD and mitochondrial topology define zones in the lobule. (A) Confocal image of a liver lobule from mtDendra2 (green) transgenic mouse. Actin was labeled with phalloidin (yellow), and lipid droplets with LipidTox (magenta). A representative PP-PC axis is marked with a dotted rectangle. **(B)** Segmentation of hepatocytes guided by actin and mitochondria labeling. **(C)** Color map representing the spatial positioning of hepatocytes based on their distance from the central vein. Scale bar 100μm. **(D)** Segmentation of lipid droplets and mitochondria within cells. Scale bar

443 5μm**. (E)** Quantification of PP-PC axis length and number of hepatocytes per axis. Data presented
444 as mean ± SD from 18 PP-PC axes analyzed from three mice (Supplementary data 1). Statistical
445 significance was calculated using a two-tailed unpaired Student's *t*-test. **(F-H)** Quantification of
446 morphological features, including mitochondrial sphericity, mitochondrial density, LD count, and
447 LD area. **(H)** Quantification of average hepatocyte cell area across the PP-PC axis. **(I)** Principal
448 Component Analysis plot of hepatocyte (R1-R12) clustering. Data presented as mean ± SD.
449
450 **Extended Figure 1. Anatomical landmarks guide tissue orientation in scPhenomics. (A)**
451 Anatomical organization of the mouse liver lobule. The model was created with Biorender.com.
452 Representative confocal images of whole lobule (left), PP-PC axes (middle), and close-up on PP
453 hepatocytes (right), from mtDendra2 transgenic mice fed a control (CNTR) diet **(B)**, overnight
454 fasted **(C)**, or Western Diet (WD) **(D)**. Mitochondria are shown in green, actin was labeled with
455 phalloidin (yellow), LDs were labeled with LipidTox (magenta), and the PP marker E-cadherin is
456 shown in cyan. Arrowheads point at actin-rich structures in the portal regions that also label with
457 E-cadherin. Scale bar 100 μm. **(E)** mtDendra2 fluorescence intensity is shown across space and
458 dietary conditions. Data is presented as mean ± SD from 18 PP-PC axes analyzed from three mice
459 (Supplementary data 1). **(F)** Liver sections from Dendra2 mice fed, fasted, or WD-fed were labeled
460 with DAPI (white), HNT4a (red), and actin (yellow). The proportion of hepatocytes ($HNF4a^+/DAPI^+$
461 cells) across three PP-PC axes was calculated. PV: portal vein; CV: central vein; PP: periportal; PC:
462 pericentral; LD: Lipid droplets
463
464 **Extended Figure 2. Single-cell analysis of LD and mitochondrial structure in 3D. (A)**
465 Representative projection of a z-stack from mtDendra2 mice showing mitochondria (green), LDs
466 (magenta), and actin (yellow). Scale bar 10 μm. **(B)** 3D surfaces depicting mitochondria (green),
467 LDs (magenta), and actin (yellow) at single-cell resolution. Cells are numbered 1 to 12 along the
468 PP-PC axis. Scale bar 2 μm. **(C)** Analysis of mitochondrial sphericity and density. **(D)** Analysis of LD
469 volume and count. **(E)** Analysis of cell volume. **(F)** Schematic representation of mitochondria and
470 LDs phenotypes along the PP-PC axis. The schematic was created with Biorender.com. A

471 representative lobule is shown; similar trends were observed in 3 independent experiments. PV:
472 portal vein; CV: central vein; LD: lipid droplet.
473
474 **Figure 2. Increased lipid flux induces rewiring of LD and mitochondria circuits. (A-C)**
475 Representative confocal images of PP-PC axes from mtDendra2 transgenic mice fed control
476 (CNTR) diet, overnight fasted or Western Diet (WD). Mitochondria are shown in green, actin was
477 labeled with phalloidin (yellow), and lipid droplets were labeled with LipidTox (magenta). Per
478 condition, representative PP and PC cells are shown in enlarged insets. Scale bar 5μm **(D-E**) LD
479 and mitochondria features, including area (total and average per cell), count, circularity, intensity,
480 perimeter, minimal distance, and density, are shown across space and dietary conditions.
481 scPhenomics data is presented as mean ± SD from 18 PP-PC axes analyzed from three mice
482 (Supplementary data 1). PV: portal vein; CV: central vein; PP: periportal; PC: pericentral; LD: Lipid
483 droplets
484
485 **Extended Figure 3. Hepatic steatosis and DNL in short-term WD feeding. (A)** Confocal images of
486 liver sections from C57BL/6J mice fed either a CNTR or WD, as indicated. LDs were labeled with
487 LipidTox (white). **(B)** Liver sections from mice fed either CNTR or WD for 4 weeks stained with
488 H&E. Scale bar 100 μm. **(C)** Relative expression levels of lipogenesis enzymes (Fasn, Acaca, Acly,
489 Scd1) and transcription factors (Srebp1c, ChREBP, and LXRa) in control diet (CNTR), fasted, or 4-
490 week WD-fed mice. Data are presented as mean ± SD from n=5 independent experiments.
491 Statistical significance was determined using a one-way ANOVA, with a Bonferroni post hoc test
492 was employed to correct for multiple comparisons. LD: lipid droplets; PP: periportal; PC:
493 pericentral; CNTR: control; WD: Western diet; DNL: de novo lipid synthesis.
494
495 **Figure 3. scPhenomics informs of cellular states and zonation of lipid metabolism**
496 Principal Component Analysis (PCA) plots of single-cell organelle features (R1-R12) under
497 different dietary conditions in **(A)** two dimensions (2D) and **(B)** three dimensions (3D). **(C)**
498 Heatmap showing single-cell (R1-R12) organelle features under different dietary conditions. **(D)**
499 Correlation Matrix Heatmap of organelle features under different dietary conditions. **(E)** Heat

500 map of mitochondria and LDs overlapping pixels across the PP-PC axis (R1-R12) and diets. All plots
501 were created with data in Supplementary data 1.
502
503 **Figure 4. Fasting-induced remodeling of the hepatic proteome in spatially sorted hepatocytes**
504 **(A)** Volcano plot showing the PP or PC, fast-to-fed log2 fold-change (x-axis), and the -log10 p-value
505 (y-axis) for identified proteins. Color coding highlighting significance based on p-value and fold
506 change. Proteomics data were analyzed using the Limma R package (version 3.40.6). **(B)** Lipid
507 pathways in hepatocytes. The schematic was created with Biorender.com. **(C-E)** Heatmaps of
508 proteins involved in lipid metabolic pathways **(C)**, mitochondrial dynamics and structure **(D)**,
509 mitochondria-LD interactions, and LD formation **(E)** across PP and PC sorted hepatocytes from fed
510 and fasted mice. Heatmap values were derived from the means of three independent
511 experiments and normalized to the total protein expression in livers from fed mice. (**F)** Western
512 blot analysis of PLIN5 levels under different dietary conditions. Statistical significance was
513 calculated using two-tailed unpaired Student's *t*-test from n=5 independent experiments.
514
515 **Extended Figure 4. Comparative proteomics of spatially sorted hepatocytes. (A)** Principal
516 component analysis (PCA) of spatially sorted hepatocytes from fed (n=4 mice) and fasted mice
517 (n=3 mice). Volcano plot showing the PC to PP log2 fold-change (x-axis) and the -log10 p-value (y-
518 axis) for identified proteins in fed **(B)** and fasted **(C)**. PP and PC proteins are shown in red and blue
519 in fed, or light red and light blue in the fasted mice, respectively. **(D)** Venn diagram illustrating PP
520 or PC signature proteins in fed and fasted mice. **(E)** GO enrichment analysis for the proteomics
521 data in the spatially sorted cells.
522
523 **Extended Figure 5. Fasting induces mitochondria-LD interactions. (A)** Confocal images of liver
524 sections from mtDendra2 (green) transgenic mice fed control, WD, or overnight fasted or WD-
525 fed-overnight fasted. LDs were labeled with Lipidtox (magenta) and actin with phalloidin (yellow).
526 Colocalization between mitochondria and LD is shown in white. Scale bar 3μm. **(B)** Mitochondria-
527 LD colocalization was quantified as the overlapping pixels normalized to the area under different
528 dietary conditions. Data presented as mean ± SD from n=5 independent experiments. Statistical

529 significance was calculated using one-way ANOVA and Bonferroni correction for multiple
530 comparisons. **(C)** Localization of endogenous PLIN5 in liver sections from fed and fasted Dendra2
531 mice. WD: western diet; LD: lipid droplets.
532
533 **Figure 5. Mitochondria-LD contacts promote LD expansion. (A)** Experimental design schematic.
534 **(B)** Representative confocal images of periportal (PP), mid-lobular (M), and pericentral (PC)
535 hepatocytes from mtDendra2 (green) mice fed a control diet (CNTR) and overexpressing PLIN5
536 variants. Actin is labeled with phalloidin (yellow), and LDs are labeled with LipidTox (magenta).
537 Scale bar 5μm. **(C)** scPhenomics of LD features, including total area, density, and count, across the
538 PP-PC axis from mice overexpressing PLIN5 variants. **(D)** scPhenomics of mitochondrial features,
539 including area and circularity, across the PP-PC axis from mice overexpressing PLIN5 variants.
540 scPhenomics data is presented as mean ± SD from 12 PP-PC axes analyzed from two mice. **(E)** Heat
541 map of mitochondria and LDs overlapping pixels across the PP-PC axis (R1-R12) from mice
542 overexpressing PLIN5 variants.
543
544 **Extended Figure 6. *In vivo* remodeling of mitochondria-LDs interactions using PLIN5 variants**
545 **overexpression. (A)** Representative confocal images of liver sections from control (CNTR) diet-fed
546 mice overexpressing PLIN5 variants. Images show mitochondria (green), LDs (magenta), and actin
547 (yellow). Scale bar 20 μm. PV: portal vein; CV: central vein. WT: wild type.
548
549 **Figure 6. Mitochondria-LD contacts promote lipid storage, reducing WD-induced lipotoxicity.**
550 **(A)** Representative confocal images of periportal (PP), mid-lobular (M), and pericentral (PC)
551 hepatocytes from mtDendra2 (green) mice fed a Western Diet (WD) and overexpressing PLIN5
552 variants. Actin is labeled with phalloidin (yellow), and LDs are labeled with LipidTox (magenta).
553 Scale bar 5μm. **(B)** Heat map of mitochondria and LDs overlapping pixels across the PP-PC axis
554 (R1-R12) from WD-fed mice overexpressing PLIN5 variants. Triglyceride **(C)** and free fatty acids
555 (FFA) **(D)** were measured in the livers of mice overexpressing PLIN5 variants, fed either CNTR or
556 WD. Statistical significance was calculated with two-way ANOVA and Tukey's test to correct for
557 multiple comparisons. Data presented as mean ± SD from $n = 10$ independent experiments.

558 Malondialdehyde (MDA) **(E)**, NADP/NADPH **(F)**, and reduced glutathione (GSH) **(G)** were
559 measured in the livers of mice overexpressing PLIN5 variants, fed either CNTR or WD. Values are
560 presented as WD/CNTR diet ratios. For each assay, a linear model was fit with diet (CNTR vs.
561 WD) and genotype as factors. WD effect for each variant was compared to the Null group.
562 Within each variant group, WD was compared with the mean CNTR diet to test if different
563 from 1 (*q<0.15; **q<0.01; ***q<0.01). Moderated t-statistics and associated p-values were
564 obtained using empirical Bayes shrinkage (eBayes). Multiple testing correction was applied
565 across assays using the Benjamini–Hochberg method, and adjusted p-values (q-values) are
566 reported.
567
568 **Extended Figure 7. Overexpression of PLIN5 variants in WD-fed mice. (A)** Representative
569 confocal images of liver sections from Western Diet (WD)-fed mice overexpressing PLIN5 variants.
570 Images show mitochondria (green), LDs (magenta), and actin (yellow). Scale bar 20 μm. **(B)**
571 Weight gain in mice overexpressing PLIN5 variants and fed CNTR or WD (n=10 mice per diet).
572 Serum FA **(C)**, cholesterol **(D),** and glucose **(E)** levels in mice overexpressing PLIN5 variants and
573 fed CNTR or WD (n=5 per diet). Data presented as mean ± SD, statistical significance was
574 calculated with two-way ANOVA and Tukey's test to correct for multiple comparisons. PV: portal
575 vein; CV: central vein; WT: wild type. CNTR: control; WD: western diet; FA: fatty acid.
576
577 **Extended Figure 8. The effect of PLIN5 variants and WD on DNL. (A)** Relative expression of mRNA
578 levels of lipogenesis enzymes Fatty acid synthase (Fasn), Acetyl-CoA carboxylase 1 (Acaca), ATP
579 citrate lyase (Acly), Stearoyl-CoA desaturase-1 (Scd1) in mice overexpressing PLIN5 variants fed a
580 control diet (CNTR), or 4-week WD-fed. Data presented as mean ± SD from n=5 independent
581 experiments. Statistical significance was calculated using a two-way ANOVA and Tukey's test to
582 correct for multiple comparisons. **(B)** Fatty acid synthase (FASN) expression levels in mice
583 overexpressing PLIN5 variants and fed CNTR or WD (n=10 mice per diet). **(C)** Relative
584 phosphorylated Acetyl-CoA carboxylase 1 (ACC1) and phosphorylated hormone-sensitive lipase
585 (HSL) in mice overexpressing PLIN5 variants fed a control diet (CNTR), or 4-week WD-fed. Data
586 presented as mean ± SD from n=10 independent experiments. Statistical significance was

587 calculated using a two-way ANOVA and Tukey's test to correct for multiple comparisons.
588 Representative Western blots are shown. DNL: de novo lipid synthesis; PV: portal vein; CV: central
589 vein; WT: wild type. CNTR: control; WD: western diet.
590
591 **Figure 7. Mitochondria-LD contacts are associated with higher lipid content in the human liver.**
592 **(A)** Histopathological summary of 12 healthy liver samples. Color coding indicates grouping based
593 on the degree of steatosis. **(B)** Oil-red-o staining of a representative individual from each group.
594 **(C)** Immunofluorescence staining of mitochondria (green), LDs (magenta), actin (yellow), and GS
595 (white) in a liver section from a representative individual with minimal or mild steatosis. **(D)**
596 Volume rendering of mitochondria (green), LDs (magenta), and actin (yellow) in a representative
597 PP and PC hepatocytes from patients with minimal or mild steatosis. Colocalizing pixels are shown
598 in white. Quantification of LD count per cell **(E)**, LD volume **(F)**, colocalization **(G)**, and PLIN5
599 expression levels **(H).** Data presented as mean ± SD from n=3 (none); n=2 (minimal); and n=3
600 (mild) patients. Each dot in E-G represents a cell. Statistical significance was calculated using a t-
601 test. PV: portal vein; CV: central vein.
602
603 **Extended Figure 9. Increased mitochondria-LD interactions correlate with prolonged WD-**
604 **feeding in mice. (A)** Representative confocal images of liver sections from mtDendra2 mice fed
605 WD for 4, 8, and 12 weeks. Mitochondria (green), LDs (magenta), and actin (yellow). Scale bar 5
606 μm. **(B)** Heat map of mitochondria and LDs overlapping pixels across the PP-PC axis (R1-R12) and
607 prolonged WD feeding. **(C)** Relative PLIN5 mRNA expression in mice fed WD for 4,8, and 12 weeks.
608 Data presented as mean ± SD from n=3 independent experiments. Statistical significance was
609 calculated using a two-way ANOVA and Tukey's test to correct for multiple comparisons. PV: portal
610 vein; CV: central vein. WT: wild type.
611
612 **Figure 8. PLIN5-induced mitochondria-LD contacts regulate lipid homeostasis.** Proposed model
613 of mitochondria-LD contacts regulation by PLIN5. PLIN5 induces mitochondria-LD contacts in a
614 phosphorylation-dependent manner. PLIN5 S155A induces contact sites promoting the
615 esterification of FFA to form TG and storage in LDs, which is protective from oxidative stress due

616 to increased dietary lipids. In PLIN5 S155E, mitochondria and LDs are rarely associated, LDs are
617 smaller, and antioxidant capacity is reduced. In long-term WD feeding, the abundance of
618 mitochondria-LD contacts increases, suggesting that the assembly of these contacts may be part
619 of an adaptive response. The model was created with Biorender.com.
620
621 **Supplement Figure 1. *In vivo* overexpression of PLIN5. (A)** Relative Plin5 mRNA expression in
622 mouse livers is presented as the mean ± SEM from n=10 mice. **(B)** Representative immunoblot
623 and quantification of PLIN5 protein levels from one mouse per group. An antibody generated
624 against the human PLIN5 carboxy terminus (upper panel) detects endogenous and exogenous
625 full-length PLIN5 but does not detect the CΔ (1-424) variant. PLIN5 levels are relative to
626 endogenous in the Null CNTR mouse. An antibody generated against amino acids within the
627 amino terminus of human PLIN5 (lower panel) detects all forms of exogenous PLIN5 but does not
628 detect endogenous levels in Null CNTR mice. PLIN5 levels are relative to WT exogenous levels in
629 CNTR mice. Full-length PLIN5 migrates at 50 kDa and the CΔ (1-424) PLIN5 migrates below 50 kDa.
630 An intense non-specific >50kDa band is present in all samples and a <50kDa band of
631 undetermined origin is seen in WD-fed mouse samples.
632
633 **Materials and methods**
634 **Animal experiments**
635 Experiments were approved by the Institutional Animal Care and Use Committee of the National
636 Cancer Institute and in compliance with the Guide for the Care and Use of Laboratory Animals
637 (National Institutes of Health publication 86-23, revised 1985). All experiments were conducted
638 on ad libitum-fed on normal chow diet (NIH-31 Open Formula) or western diet (TD.120528,
639 Envigo), four to ten weeks old C57BL/6J (strain# 000664) or mtDendra2 excised [20] (photo-
640 activatable mitochondria; strain# 018397) male mice obtained from Jackson Laboratories.
641 **Intra-cardiac fixation, tissue processing, and immunofluorescence**
642 Mice were anesthetized with 250 mg/kg Xylazine and 50 mg/kg Ketamine (diluted in saline)
643 injected intraperitoneally (i.p.). The liver was fixed by transcardial perfusion of ice-cold PBS for 2
644 min followed by ice-cold 4% paraformaldehyde (PFA) in PBS at a rate of 5 ml/min. Livers were

645 harvested and stored in 4% PFA in PBS overnight and processed in a sucrose gradient before
646 embedding in OCT (Tissue-Tek). Blocks were kept at -80 °C until 10 μm thick slices were made
647 with a cryostat and slides prepared. Slides were stored at -80 °C until thawed, rehydrated, and
648 blocked with 0.1% Triton X-100 and 10% FBS in PBS for 1 h at room temperature. Next, slides were
649 incubated with primary antibody at 4 °C overnight. The following day, the slides were washed
650 three times, 15 min each, and then incubated with a secondary antibody for 1 h at room
651 temperature. After three 15 min washes, slides were mounted with Fluoromount-G and a
652 coverslip (#1).

653 **Confocal microscopy and scPhenomics**

654 Tile scans and z stacks were acquired using a Leica SP8 inverted confocal laser scanning
655 microscope using a 63x oil objective and a 1.4 numerical aperture.

656 Whole lobule images were analyzed using a custom Python script (Python v. 3.10) using the deep-
657 learning Cellpose package for segmentation [21]. Individual hepatocytes were identified by first
658 creating a combination channel of actin and Gaussian-blurred mitochondria. We applied a
659 custom-trained Cellpose model to this combination channel to generate hepatocyte segments.
660 The central and portal veins were manually segmented, and their total length was measured.
661 Segmented hepatocyte distance to the central vein was normalized to the total PP-PC length and
662 then binned into 12 regions to ensure at least one hepatocyte per bin. Code will be available upon
663 publication.

664 Mitochondria and lipid droplets were segmented using their own custom-trained Cellpose
665 models. Lipid droplet segments were also subjected to an intensity threshold to remove false-
666 positive segments. The mitochondria and lipid droplet segments were used to quantify organelle
667 counts per cell, densities, mitochondrial and lipid fluorescence intensities, as well as geometric
668 parameters, including total and average area, average perimeter, circularity, eccentricity, solidity,
669 and ferret diameter using the region props function from scikit-image [55]. The shortest
670 mitochondria to lipid droplet distance, percent mitochondria/lipid droplet overlap, and
671 mitochondria Circularity = 4*pi*area / perimeter^2 were quantified.

672 Principal Component Analysis (PCA) was performed using FactoMineR ver.2.11 R package. The
673 following variables were used in calculations: counts, Total Area, Average Area, Average

674 Perimeter, Average Eccentricity, Average Solidity, Average Feret, Average Mito Int, Average Lipid
675 Int, Average Organelle Min Dist, Average Circularity, and Average Density. Unsupervised clustering
676 was performed using the hclust (method = "complete") command of stats ver. 4.3.0 R package
677 and heatmap were visualized using pheatmap ver 1.0.12. Correlation values were calculated with
678 default settings ("cor" command of "stats" R package), rounded to 2 decimal places, and
679 visualized using the ggplot function.
680 For 3D evaluation, surfaces were generated using Imaris (Bitplane 9.9.0) for mitochondria, lipid
681 droplets, and the whole cell. Geometrical measurements were exported into Excel.
682 **Histology**
683 Mouse liver tissues were also used for independent histological analysis of liver steatosis with
684 hematoxylin and eosin (H&E) by Histoserv (Germantown, MD).
685 **Liver perfusion and hepatocyte isolation**
686 Livers of anesthetized mice were perfused by inserting a 22-gauge syringe into the portal vein and
687 delivering 25 ml of pre-warmed (37 °C) perfusion buffer [Krebs-Henseleit buffer (Sigma) with 0.5
688 µM EDTA], followed by 50 ml collagenase A buffer [Krebs-Henseleit buffer, with 0.1 mM Ca2Cl and
689 0.4 mg/ml collagenase A (Sigma)]. After perfusion, livers were transferred into a Petri dish,
690 flooded with cold PBS and hepatocytes gently released using forceps. Dissociated cells were
691 collected and filtered through a 100 µm cell strainer. Cells were centrifuged at 50 rpm for 5 min
692 at 4 °C to obtain a hepatocyte enriched pellet. Pellets were resuspended in cold PBS, filtered
693 through a 40 µm cell strainer and centrifuged at 50 rpm for 5 min at 4 °C. Percoll diluted in 10x
694 Hank's buffer (Sigma) was added to cell suspension and centrifuged at 50 rpm for 5 min at 4 °C.
695 and the supernatant containing dead cells was removed by aspiration. The pellet was
696 resuspended in cold PBS and cell number determined.
697 **Fluorescence-activated cell sorting (FACS) of PP and PC populations.**
698 Cell sorting was performed on a FACSAria Fusion cell sorter (BD Biosciences). Forward and side
699 light scatter was used to distinguish cells from debris and to identify single cells. Zombie-Green
700 fixable live dead dye (1:500, BioLegend) was used to discriminate live and dead cells. The PP and
701 PC populations were identified using anti-E-cadherin-PE and anti-CD73-APC antibody staining

702 (1:150; BioLegend). The PP- and PC-specific gates were set after spectral compensation using
703 appropriate fluorescent minus (FMO) controls.

704 **Protein Digestion and TMT labeling**

705 Cells were lysed in 50 mM HEPES, pH 8.0, 8M urea, and 10% methanol, followed by sonication.
706 Lysates were clarified by centrifugation and protein concentration was quantified using a BCA
707 protein estimation kit (Thermo Fisher). A 250 ug was alkylated and digested by incubating
708 overnight at 37oC in trypsin at a ratio of 1:50 (Promega). Digestion was acidified by adding formic
709 acid (FA) to a final concentration of 1% and desalted using Pierce peptide desalting columns
710 according to the manufacturer's protocol. Peptides were eluted from the column using 50%
711 ACN/0.1% FA, dried in a speedvac and kept frozen at -20oC for further analysis.

712 For TMT labeling, 125 ug of each sample was reconstituted in 50 μl of 50 mM HEPES, pH 8.0, 500
713 ug of TMTpro-16plex label (Thermo Fisher) in 100% ACN. After incubating the mixture for 1 h at
714 room temperature with occasional mixing, the reaction was terminated by adding 8 ⍰l of 5%
715 hydroxylamine. As there were more than 16 samples, we generated a pooled sample consisting
716 of equal amounts of lysate from each condition and TMT labeled. The pool was added to each
717 TMT experiment. The TMT-labeled peptides were pooled and dried in a speedvac. The samples
718 were desalted, and excess TMT label was removed using peptide desalting columns (Thermo
719 Fisher). A 100 ug aliquot of labeled peptide mixture was fractionated using a high pH reversed
720 phase.

721 **High pH reversed-phase fractionation.**

722 The first-dimensional separation of peptides was performed using a Waters Acquity UPLC system
723 coupled with a fluorescence detector (Waters) using a 150 mm x 3.0 mm Xbridge Peptide BEMTM
724 2.5 μm C18 column (Waters) operating at 0.35 ml/min. The dried peptides were reconstituted in
725 100 μl of mobile phase A solvent (3 mM ammonium bicarbonate, pH 8.0). Mobile phase B was
726 100% acetonitrile (Thermo Fisher). The column was washed with mobile phase A for 10 min
727 followed by gradient elution 0- 50% B (10-60 min) and 50-75 %B (60-70 min). Fractions were
728 collected every minute. These 60 fractions were pooled into 24 fractions. Fractions were vacuum
729 centrifuged, and lyophilized fractions were stored at -80°C until analysis by mass spectrometry.

730 **Mass Spectrometry acquisition**

731 The lyophilized peptide fractions were reconstituted in 0.1% TFA and subjected to nanoflow liquid
732 chromatography (Thermo UltimateTM 3000RSLC nano LC system, Thermo Fisher) coupled to an
733 Orbitrap Eclipse mass spectrometer (Thermo Fisher). Peptides were separated using a low pH
734 gradient using a 5-50% ACN over 120 min in a mobile phase containing 0.1% formic acid at 300
735 nl/min flow rate. MS scans were performed in the Orbitrap analyzer at a resolution of 120,000
736 with an ion accumulation target set at 4e5 and max IT set at 50ms over a mass range of 400-1600
737 m/z. Ions with a determined charge state between 2 and 5 were selected for MS2 scans in the ion
738 trap with CID fragmentation (Turbo; NCE 35%; maximum injection time 35 ms; AGC 1 × 104). The
739 spectra were searched using the Real Time Search Node in the tune file using mouse Uniprot
740 database using Comet search algorithm with TMT16 plex (304.2071Da) set as a static modification
741 of lysine and the N-termini of the peptide. Carbamidomethylation of cysteine residues
742 (+57.0214 Da) was set as a static modification, while oxidation of methionine residues
743 (+15.9949 Da) was set up as a dynamic modification. For the selected peptide, an SPS–MS3 scan
744 was performed using up to 10 b- and y-type fragment ions as precursors in an Orbitrap at 50,000
745 resolution with a normalized AGC set at 500 followed by maximum injection time set as "Auto"
746 with a normalized collision energy setting of 65.

747 **Data Analysis**

748 Acquired MS/MS spectra were searched against the mouse Uniprot protein database along with
749 a contaminant protein database using SEQUEST in the Proteome Discoverer 2.4 software (Thermo
750 Fisher). The precursor ion tolerance was set at 10 ppm and the fragment ions tolerance was set
751 at 0.02 Da, with methionine oxidation included as a dynamic modification**.**
752 Carbamidomethylation of cysteine residues and TMTpro16 plex (304.2071 Da) were set as static
753 modification of lysine and the N-terminus of the peptide. Trypsin was specified as the proteolytic
754 enzyme, with up to 2 missed cleavage sites allowed. Searches used a reverse sequence decoy
755 strategy to control for the false peptide discovery and identifications were validated using the
756 Percolator algorithm in Proteome Discoverer 2.4.

757 Reporter ion intensities were adjusted to correct for lot-specific impurities according to the
758 manufacturer specification and the abundances of the proteins were quantified using the
759 summation of the reporter ions for all identified peptides. A two-step normalization procedure

760 was applied on a 24-plex TMT experiment [2 TMT experiments with 12 samples each]. First, the
761 reporter abundances were normalized across all the channels to account for equal peptide
762 loading. Secondly, the intensity from the pooled sample was used to normalize the batch effect
763 from the multiple TMT experiments. Samples were further normalized using the voom algorithms
764 and quantile normalization from the Limma R package (v3.40.6). Differential peptide expression
765 analysis was performed using Limma, where zonation was determined by the p-value (0.05)
766 and/or FC (≥1.2); and pathway enrichment analysis was performed using Fisher's Exact test with
767 GO database. Graphpad Prism 9 and Biorender was used for visualization.
768 The mass spectrometry dataset will be available upon publication.

769 **Seahorse assay**

770 A Seahorse XFe96 Analyzer and XF Mito Stress Test Kit (Agilent Technologies) was used to measure
771 the oxygen consumption rate (OCR) and extracellular acidification rate (ECAR) of PP and PC sorted
772 cells. A day prior to the assay, the cartridge sensor was hydrated overnight with Seahorse
773 Bioscience Calibration Solution at 37 °C without CO2. After sorting, cells were seeded in a 96-well
774 seahorse plate at a density of 5.0 × 104 cells/well and allowed to adhere for 2 h. After 2 h, cell
775 media was replaced with serum-free Seahorse XF Base media containing glucose, pyruvate, and
776 glutamine (pH 7.4), and the cells were incubated at 37 ℃ in a non-CO2 incubator for 1 h. OCR and
777 ECAR were measured after the injection of oligomycin (1.5 μM), FCCP (1 μM), and
778 rotenone/antimycin (0.5 μM). Four independent experiments were conducted with six to eight
779 replicates per population and treatment condition per experiment. All data was normalized to
780 BCA (Thermo Fisher). Measurements for basal respiration and maximum respiration capacity
781 were presented as a percentage normalized to PP fed.

782 **Overexpression of PLIN5 variants in mice**

783 Four-week-old C57BL/6 J male mice and mtDendra2 excised male mice were housed five per cage
784 in a facility (12 h light/dark cycle) and fed either a control chow diet (NIH-31 Open Formula) or
785 Western Diet (WD; TD.120528, Envigo) for two weeks. Mice were then injected via tail vein with
786 an AAV8-ABLp vector: Null, mPlin5 WT, S155A, S155E, CΔ (1-424), driven by a liver-specific
787 albumin promoter, at a titer of 4.5× 10^{11} GC (Vector Biolabs, Philadelphia, PA). After AAV8

788 transduction, mice were fed the control chow diet or WD for four weeks. At the end of the
789 experiment, serum and liver tissue were collected.

790 **Serum analysis**

791 Kits were used according to manufacturer's instructions to measure β-hydroxybutyrate (Abcam),
792 free fatty acid FUJIFILM (Wako Diagnostics), triglycerides (Pointe Scientific), cholesterol (Thermo
793 Scientific), insulin (Crystal Chem Inc).

794 **Blood Glucose**

795 Blood was collected from the tail vein, and glucose was measured using testing strips and monitor
796 (Ascencia Diabetes Care).

797 **Triglyceride (TG), Malondialdehyde (MDA), and Glutathione measurements**

798 Pulverized liver tissue samples were lysed, and the supernatant was collected after centrifugation
799 at 13,000 rpm for 10 minutes. Triglyceride levels were measured with a Colorimetric Assay Kit
800 (Elabscience), Cellular Malondialdehyde (MDA) levels were measured with a Lipid Peroxidation
801 (MDA) Assay Kit (Abcam), NADP/NADPH (Sigma MAK479), and total cellular glutathione (GSH)
802 levels were estimated through the GSH Glo™ Assay Kit (Promega). Each kit was used per the
803 manufacturer's instructions, and results were normalized to protein amount, and absolute
804 numbers were converted to fold change.

805 **Western blot analysis**

806 Proteins from primary hepatocytes or pulverized liver were extracted by homogenization in RIPA
807 lysis buffer (150 mM NaCl, 0.1% Triton X-100, 0.5% sodium deoxycholate, 0.1% sodium dodecyl
808 sulfate, and 50 mM Tris HCl pH 8.0) containing EDTA, PMSF, and Halt Inhibitor Cocktail (Thermo
809 Fisher), followed by centrifugation at 13,000 rpm at 4 °C for 30 min. Protein concentration was
810 determined using a Pierce™ BCA Protein Assay Kit (Thermo Fisher). Lysates were boiled at 95 °C
811 for 5 min, and 5-10 μg aliquots were fractionated by SDS-PAGE and then transferred to
812 nitrocellulose 0.45 μm membrane (Bio-Rad). Membranes were blocked for 1 h at room
813 temperature in 5% non-fat milk in 1x Tris-buffered saline + 0.1% Tween 20 (TBST) then incubated
814 with primary antibody diluted in 5% BSA in 1x TBST at 4 °C overnight. Membranes were washed
815 three times with TBST, then incubated in the secondary antibody diluted in 5% non-fat milk in 1x
816 TBST for 1 h at room temperature. Membranes were washed three times with TBST, and then

817 Clarity ECL Western blot substrate solution (Bio-Rad) was applied for detection. The membranes
818 were imaged using the ChemiDoc Imaging System (Bio-Rad). Bands were quantified with
819 ImageLab (Bio-Rad).

820 **RNA isolation and Quantitative PCR**

821 RNA was isolated from pulverized liver tissue using the TissueLyser LT and RNeasy mini kit
822 (Qiagen). A High-Capacity RNA to cDNA kit (Thermo Fisher) was used to synthesize random-
823 primed cDNA from 2 µg DNAse treated RNA. Real time PCR was conducted in 384 well-plates
824 using a ViiA7 Real-Time PCR system (Applied Biosystems). Singleplex reactions (5 µl) containing a
825 FAM-MGB expression assay for Plin5 (Mm00508854_m1) or Tbp control (Mm01277041_m1)
826 (Thermo Fisher) were performed using cDNA synthesized from 8 ng RNA and 1× Fast Advanced
827 Master Mix (Thermo-without Amp Erase UNG) were performed in triplicate. The comparative Ct
828 method (delta, delta Ct) was used to determine relative expression normalized to Tbp (Applied
829 Biosystems® ViiA™ 7Real-Time PCR System Getting Started Guides).

830 **Human liver sample collection**

831 Human tissue was acquired with informed consent under an NIH IRB-approved protocol
832 (NCT01915225) during risk-reducing surgery performed on patients with germline mutation in
833 the tumor suppressor CDH1. Mutations in CDH1 are a frequent cause of the hereditary diffuse
834 gastric cancer (HDGC) syndrome, which is associated with gastric adenocarcinoma, lobular breast
835 cancer, and cleft lip/palate. These patients undergo risk-reducing total gastrectomy, and some
836 consent to a liver biopsy during the surgery. While these patients often have microscopic stage
837 1A cancers, none had deeply invasive or metastatic carcinoma in their livers.

838 The tissue procured was characterized as normal upon visible inspection, followed by
839 histopathological evaluation. Tissue was procured within approximately 20 minutes of the
840 incision and then fixed in 1% PFA in PBS for 48 or 72 hours. It was then washed in PBS and
841 incubated in 30% sucrose in PBS for at least 24 hours before being embedded in OCT. OCT blocks
842 were stored at -80 °C.

843 **Statistical analyses of MDA, GSA, and NADP/NADPH**

844 All assay values were $\log_2$-transformed prior to modeling. Statistical analyses were performed in
845 R using the limma package. For each metabolite, a linear model was fit with diet (control diet, CD

846 vs. Western diet, WD) and genotype as factors. Two sets of contrasts were tested. The first was
847 to assess whether the WD effect in each genotype differed from that in the Null group, where
848 contrasts were constructed as (WD – CD for each genotype) – (WD – CD for Null). This evaluates
849 whether the magnitude of the WD–CD change deviates significantly from the corresponding
850 change in the Null genotype. The second was to test within-genotype WD vs. CD, where WD
851 samples were compared against the mean of CD samples of the same genotype to test whether
852 the $\log_2$(WD/CD) ratio differed from zero (i.e., whether the linear WD/CD fold change differed
853 from 1). Moderated t-statistics and associated p-values were obtained using empirical Bayes
854 shrinkage (eBayes). Multiple testing correction was applied across assays using the Benjamini–
855 Hochberg method, and adjusted p-values (q-values) are reported.
856
857 **Supplement table 1:**

Antibodies	Source	Identifier	Dilution
APC anti-mouse CD73 antibody	Biolegend	127210	1:150
Alexa Fluor® 594 anti-mouse/human CD324 (E-Cadherin) Antibody	Biolegend	147306	1:100
Anti-mouse IgG, HRP-linked Antibody	Cell Signaling	3662S	1:2500
Anti-rabbit IgG, HRP-linked antibody	Cell Signaling	7076S	1:10000
Cyclophilin B (D1V5J) Rabbit monoclonal antibody	Cell Signaling	43603S	1:1000
Phospho-HSL (Ser565) Antibody	Cell Signaling	4137S	1:1000

β-Actin (13E5) Rabbit monoclonal antibody	Cell Signaling	4970S	1:1000
β-actin (8H10D10) Mouse monoclonal antibody	Cell Signaling	3700S	1:1000
β-tubulin (9F3) Rabbit monoclonal antibody	Cell Signaling	2128S	1:1000
Goat anti-Rabbit IgG (H+L) Cross-Absorbed Secondary Antibody, Alexa Fluor 568	Invitrogen™	A11011	1:400
Alexa Fluor™ 568 Phalloidin	Invitrogen™	A12380	1:100
Alexa Fluor™ 647 Phalloidin	Invitrogen™	A22287	1:100
Perilipin 5 Polyclonal antibody	Proteintech	26051-1-AP	1:2000
OXPAT Polyclonal Antibody	Invitrogen™	PA5-114352	1:500
GAPDH	Cell Signaling	2118S	1:1000

858

Dyes		
Alexa Fluor™ 568 Phalloidin	Thermo Fisher	A12380
HSC LipidTOX™ Deep Red Neutral Lipid Stain, for cellular imaging	Thermo Fisher	H34477
Buffers		
RIPA Lysis buffer	Thermo Fisher	J62524-AE

Thermo Scientific™ Halt™ Protease and Phosphatase Inhibitor Cocktail (100X)	Thermo Fisher	78442
Prec Plus Protein Dual Color Standards	Bio-Rad	1610374
10X Tris/Glycine/SDS	Bio-Rad	1610732
2X Laemmli Sample Buffer	Bio-Rad	1610737
Clarity Western ECL Substrate	Bio-Rad	1705061
Seahorse XF base medium, without phenol red, 500 mL	Aglient	103335-100
Seahorse XF 1.0 M glucose solution, 50 mL	Aglient	103577-100
Seahorse XF 100 mM pyruvate solution, 50 mL	Aglient	103578-100
Seahorse XF 200 mM glutamine solution, 50 mL	Aglient	103579-100
Seahorse XF Calibrant Solution 500 mL	Aglient	100840-000
Seahorse XF Cell Mito Stress Test kit	Aglient	103010-100
Seahorse XF Mito Fuel Flex Test kit	Aglient	103260-100
Collage I, Rat Tail, 100 mg	Corning	354236
Phosphate Buffered Saline, pH 7.2, 1X	Quality Biological	111-056-101
Hanks' Balanced Saline pH 7.2, 1X	Thermo Fisher	14174-095
Acetic acid	Sigma Aldrich	A6283

Collagenase from Clostridium histolyticum	Sigma Aldrich	C5138
Krebs-Henseleit Buffer Modified	Sigma Aldrich	K3753
Calcium chloride solution	Sigma Aldrich	21115
Sodium bicarbonate	Sigma Aldrich	S6014
Ethylenediaminetetraacetic acid disodium salt solution	Sigma Aldrich	03690
HEPES solution	Sigma Aldrich	H0887
Fetal Bovine Serum	Thermo Fisher	26140079
TMTpro™ 16plex Label Reagent set	Thermo Fisher	A44520
HiSelect ™ Phosphopeptide enrichment kit	Thermo Fisher	A32992
High Select TM Phosphopeptide Enrichment kit	Thermo Fisher	A32993
Trypsin Platinum	Promega	VA9000
Urea	Sigma Aldrich	51457
Methanol	Sigma Aldrich	34860
Trifluoroacetic acid	Sigma Aldrich	302031
Acetonitrile solution	Sigma Aldrich	900686
qPCR		
Plin5	Thermo Fisher	Mm00508854_m1
Tbp	Thermo Fisher	Mm01277041_m1
Taqman Fast Advanced Master Mix	Thermo Fisher	4444963

High-Capacity RNA to cDNA kit	Thermo Fisher	4388950
RNeasy mini kit	Qiagen	74104
Assay		
Pierce™ BCA Protein Assay kit	Thermo Fisher	23225
Triglyceride (TG) Colorimetric assay kit	Thermo Fisher	EEA028
NADP/NADPH assay kit	Sigma	Sigma- MAK479
Non-esterified Free Fatty Acids (NEFA/FFA) Colorimetric Assay Kit	Elabscience	E-BC-K013-M
GSH-Glo™ Glutathione Assay	Promega	V6911
Lipid peroxidation assay kit	Abcam	ab233471
Other		
Pierce™ Peptide Desalting Spin Columns	Thermo Fisher	89851
Seahorse XF96 V3 PS culture Microplates	Aglient	101085-004
Mini-Protein® TGX™ Precast Gels	Bio-Rad	4568084
Trans-Blot Turbo NC Transfer Packs	Bio-Rad	1704158

References

(1) Israelsen, M.; Francque, S.; Tsochatzis, E. A.; Krag, A. Steatotic liver disease. *The Lancet* **2024**, *404* (10464), 1761-1778. DOI: 10.1016/S0140-6736(24)01811-7 (acccessed 2025/10/07).

(2) Bosch, M.; Parton, R. G.; Pol, A. Lipid droplets, bioenergetic fluxes, and metabolic flexibility. *Semin Cell Dev Biol* **2020**. DOI: 10.1016/j.semcdb.2020.02.010.

(3) Kneeman, J. M.; Misdraji, J.; Corey, K. E. Secondary causes of nonalcoholic fatty liver disease. *Therap Adv Gastroenterol* **2012**, *5* (3), 199-207. DOI: 10.1177/1756283x11430859 From NLM.

(4) Puchalska, P.; Crawford, P. A. Multi-dimensional Roles of Ketone Bodies in Fuel Metabolism, Signaling, and Therapeutics. *Cell Metab* **2017**, *25* (2), 262-284. DOI: 10.1016/j.cmet.2016.12.022 From NLM Medline.

(5) Porat-Shliom, N. Compartmentalization, cooperation, and communication: The 3Cs of Hepatocyte zonation. *Current Opinion in Cell Biology* **2024**, *86*, 102292. DOI: https://doi.org/10.1016/j.ceb.2023.102292.

(6) Cunningham, R. P.; Porat-Shliom, N. Liver Zonation - Revisiting Old Questions With New Technologies. *Front Physiol* **2021**, *12*, 732929. DOI: 10.3389/fphys.2021.732929.

(7) Acevedo-Acevedo, S.; Stefkovich, M. L.; Kang, S. W. S.; Cunningham, R. P.; Cultraro, C. M.; Porat-Shliom, N. LKB1 acts as a critical brake for the glucagon-mediated fasting response. *Hepatol Commun* **2022**, *6* (8), 1949-1961. DOI: 10.1002/hep4.1942 From NLM Medline.

(8) Cali, T.; Bayer, E. M.; Eden, E. R.; Hajnoczky, G.; Kornmann, B.; Lackner, L.; Liou, J.; Reinisch, K.; Rhee, H. W.; Rizzuto, R.; et al. Key challenges and recommendations for defining organelle membrane contact sites. *Nat Rev Mol Cell Biol* **2025**. DOI: 10.1038/s41580-025-00864-x From NLM Publisher.

(9) Prinz, W. A.; Toulmay, A.; Balla, T. The functional universe of membrane contact sites. *Nat Rev Mol Cell Biol* **2020**, *21* (1), 7-24. DOI: 10.1038/s41580-019-0180-9.

(10) Olzmann, J. A.; Carvalho, P. Dynamics and functions of lipid droplets. *Nat Rev Mol Cell Bio* **2019**, *20* (3), 137-155. DOI: 10.1038/s41580-018-0085-z.

(11) Schuldiner, M.; Bohnert, M. A different kind of love - lipid droplet contact sites. *Bba-Mol Cell Biol L* **2017**, *1862* (10), 1188-1196. DOI: 10.1016/j.bbalip.2017.06.005.

(12) Gemmink, A.; Daemen, S.; Kuijpers, H. J. H.; Schaart, G.; Duimel, H.; López-Iglesias, C.; van Zandvoort, M. A. M. J.; Knoops, K.; Hesselink, M. K. C. Super-resolution microscopy localizes perilipin 5 at lipid droplet-mitochondria interaction sites and at lipid droplets juxtaposing to perilipin 2. *Bba-Mol Cell Biol L* **2018**, *1863* (11), 1423-1432. DOI: 10.1016/j.bbalip.2018.08.016.

(13) Kimmel, A. R.; Sztalryd, C. Perilipin 5, a lipid droplet protein adapted to mitochondrial energy utilization. *Curr Opin Lipidol* **2014**, *25* (2), 110-117. DOI: 10.1097/MOL.0000000000000057 From NLM Medline.

(14) Wang, H.; Sreenivasan, U.; Hu, H.; Saladino, A.; Polster, B. M.; Lund, L. M.; Gong, D. W.; Stanley, W. C.; Sztalryd, C. Perilipin 5, a lipid droplet-associated protein, provides physical and metabolic linkage to mitochondria. *J Lipid Res* **2011**, *52* (12), 2159-2168. DOI: 10.1194/jlr.M017939 From NLM Medline.

(15) Najt, C. P.; Khan, S. A.; Heden, T. D.; Witthuhn, B. A.; Perez, M.; Heier, J. L.; Mead, L. E.; Franklin, M. P.; Karanja, K. K.; Graham, M. J.; et al. Lipid Droplet-Derived Monounsaturated Fatty Acids Traffic via PLIN5 to Allosterically Activate SIRT1. *Mol Cell* **2020**, *77* (4), 810-824 e818. DOI: 10.1016/j.molcel.2019.12.003.

(16) Olzmann, J. A.; Carvalho, P. Dynamics and functions of lipid droplets. *Nat Rev Mol Cell Biol* **2019**, *20* (3), 137-155. DOI: 10.1038/s41580-018-0085-z From NLM Medline.

(17) Parlakgul, G.; Pang, S.; Artico, L. L.; Min, N.; Cagampan, E.; Villa, R.; Goncalves, R. L. S.; Lee, G. Y.; Xu, C. S.; Hotamisligil, G. S.; Arruda, A. P. Spatial mapping of hepatic ER and mitochondria architecture reveals zonated remodeling in fasting and obesity. *Nat Commun* **2024**, *15* (1), 3982. DOI: 10.1038/s41467-024-48272-7 From NLM Medline.

(18) Kang, S. W. S.; Cunningham, R. P.; Miller, C. B.; Brown, L. A.; Cultraro, C. M.; Harned, A.; Narayan, K.; Hernandez, J.; Jenkins, L. M.; Lobanov, A.; et al. A spatial map of hepatic mitochondria

911 uncovers functional heterogeneity shaped by nutrient-sensing signaling. *Nature Communications*
912 **2024**, *15* (1), 1799. DOI: 10.1038/s41467-024-45751-9.
913 (19) Rosenberger, F. A.; Thielert, M.; Strauss, M. T.; Schweizer, L.; Ammar, C.; Madler, S. C.;
914 Metousis, A.; Skowronek, P.; Wahle, M.; Madden, K.; et al. Spatial single-cell mass spectrometry
915 defines zonation of the hepatocyte proteome. *Nat Methods* **2023**, *20* (10), 1530-1536. DOI:
916 10.1038/s41592-023-02007-6 From NLM Medline.
917 (20) Pham, A. H.; McCaffery, J. M.; Chan, D. C. Mouse lines with photo-activatable mitochondria
918 to study mitochondrial dynamics. *Genesis* **2012**, *50* (11), 833-843. DOI: 10.1002/dvg.22050.
919 (21) Pachitariu, M.; Stringer, C. Cellpose 2.0: how to train your own model. *Nature Methods* **2022**,
920 *19* (12), 1634-1641. DOI: 10.1038/s41592-022-01663-4.
921 (22) van der Walt, S.; Schonberger, J. L.; Nunez-Iglesias, J.; Boulogne, F.; Warner, J. D.; Yager, N.;
922 Gouillart, E.; Yu, T.; scikit-image, c. scikit-image: image processing in Python. *PeerJ* **2014**, *2*, e453.
923 DOI: 10.7717/peerj.453 From NLM PubMed-not-MEDLINE.
924 (23) Softic, S.; Gupta, M. K.; Wang, G. X.; Fujisaka, S.; O'Neill, B. T.; Rao, T. N.; Willoughby, J.;
925 Harbison, C.; Fitzgerald, K.; Ilkayeva, O.; et al. Divergent effects of glucose and fructose on hepatic
926 lipogenesis and insulin signaling. *J Clin Invest* **2018**, *128* (3), 1199. DOI: 10.1172/JCI99009 From
927 NLM PubMed-not-MEDLINE.
928 (24) Rui, L. Energy metabolism in the liver. *Compr Physiol* **2014**, *4* (1), 177-197. DOI:
929 10.1002/cphy.c130024 From NLM Medline.
930 (25) Tracz-Gaszewska, Z.; Sowka, A.; Dobrzyn, P. Stearoyl-CoA desaturase 1 inhibition impairs
931 triacylglycerol accumulation and lipid droplet formation in colorectal cancer cells. *J Cell Physiol*
932 **2023**, *238* (12), 2888-2903. DOI: 10.1002/jcp.31137 From NLM Medline.
933 (26) Sun, Q.; Xing, X. R.; Wang, H. Y.; Wan, K.; Fan, R. B.; Liu, C.; Wang, Y. J.; Wu, W. Y.; Wang, Y. B.;
934 Wang, R. SCD1 is the critical signaling hub to mediate metabolic diseases: Mechanism and the
935 development of its inhibitors. *Biomed Pharmacother* **2024**, *170*. DOI: ARTN 115586
936 10.1016/j.biopha.2023.115586.
937 (27) Springer, M. Z.; Poole, L. P.; Drake, L. E.; Bock-Hughes, A.; Boland, M. L.; Smith, A. G.; Hart, J.;
938 Chourasia, A. H.; Liu, I.; Bozek, G.; Macleod, K. F. BNIP3-dependent mitophagy promotes cytosolic
939 localization of LC3B and metabolic homeostasis in the liver. *Autophagy* **2021**, *17* (11), 3530-3546.
940 DOI: 10.1080/15548627.2021.1877469 From NLM Medline.
941 (28) Droin, C.; Kholtei, J. E.; Bahar Halpern, K.; Hurni, C.; Rozenberg, M.; Muvkadi, S.; Itzkovitz, S.;
942 Naef, F. Space-time logic of liver gene expression at sub-lobular scale. *Nat Metab* **2021**. DOI:
943 10.1038/s42255-020-00323-1.
944 (29) Heijboer, A. C.; Donga, E.; Voshol, P. J.; Dang, Z. C.; Havekes, L. M.; Romijn, J. A.; Corssmit, E.
945 P. M. Sixteen hours of fasting differentially affects hepatic and muscle insulin sensitivity in mice. *J*
946 *Lipid Res* **2005**, *46* (3), 582-588. DOI: 10.1194/jlr.M400440-JLR200.
947 (30) Granneman, J. G.; Moore, H. P.; Mottillo, E. P.; Zhu, Z.; Zhou, L. Interactions of perilipin-5
948 (Plin5) with adipose triglyceride lipase. *J Biol Chem* **2011**, *286* (7), 5126-5135. DOI:
949 10.1074/jbc.M110.180711.
950 (31) Gallardo-Montejano, V. I.; Saxena, G.; Kusminski, C. M.; Yang, C.; McAfee, J. L.; Hahner, L.;
951 Hoch, K.; Dubinsky, W.; Narkar, V. A.; Bickel, P. E. Nuclear Perilipin 5 integrates lipid droplet lipolysis
952 with PGC-1alpha/SIRT1-dependent transcriptional regulation of mitochondrial function. *Nat*
953 *Commun* **2016**, *7*, 12723. DOI: 10.1038/ncomms12723 From NLM Medline.

(32) Vacca, M.; Kamzolas, I.; Harder, L. M.; Oakley, F.; Trautwein, C.; Hatting, M.; Ross, T.; Bernardo, B.; Oldenburger, A.; Hjuler, S. T.; et al. An unbiased ranking of murine dietary models based on their proximity to human metabolic dysfunction-associated steatotic liver disease (MASLD). *Nature Metabolism* **2024**, *6* (6), 1178-+. DOI: 10.1038/s42255-024-01043-6.

(33) Li, Z.; Lange, M.; Dixon, S. J.; Olzmann, J. A. Lipid Quality Control and Ferroptosis: From Concept to Mechanism. *Annu Rev Biochem* **2024**, *93* (1), 499-528. DOI: 10.1146/annurev-biochem-052521-033527 From NLM Medline.

(34) Tschuck, J.; Skafar, V.; Friedmann Angeli, J. P.; Hadian, K. The metabolic code of ferroptosis: nutritional regulators of cell death. *Trends Biochem Sci* **2025**, *50* (8), 663-676. DOI: 10.1016/j.tibs.2025.04.007 From NLM Medline.

(35) Rosenberger, F. A.; Thielert, M.; Mann, M. Making single-cell proteomics biologically relevant. *Nat Methods* **2023**, *20* (3), 320-323. DOI: 10.1038/s41592-023-01771-9 From NLM Medline.

(36) Weiss, C., Brown LA, Miranda L, Pellizzoni P, Ben-Moshe S, Steigerwald S, Remmert K, Hernandez J, Borgwardt K, Rosenberger FA*, Porat-Shliom N*, Matthias Mann* Single cell spatial proteomics maps human liver zonation patterns and their vulnerability to fibrosis. *BioRxiv* **2025**. DOI: doi: https://doi.org/10.1101/2025.04.13.648568.

(37) Zimmermann, J. A.; Lucht, K.; Stecher, M.; Badhan, C.; Glaser, K. M.; Epple, M. W.; Koch, L. R.; Deboutte, W.; Manke, T.; Ebnet, K.; et al. Functional multi-organelle units control inflammatory lipid metabolism of macrophages. *Nat Cell Biol* **2024**, *26* (8), 1261-1273. DOI: 10.1038/s41556-024-01457-0 From NLM Medline.

(38) Najt, C. P.; Adhikari, S.; Heden, T. D.; Cui, W.; Gansemer, E. R.; Rauckhorst, A. J.; Markowski, T. W.; Higgins, L.; Kerr, E. W.; Boyum, M. D.; et al. Organelle interactions compartmentalize hepatic fatty acid trafficking and metabolism. *Cell Rep* **2023**, *42* (5), 112435. DOI: 10.1016/j.celrep.2023.112435 From NLM Publisher.

(39) Miner, G. E.; So, C. M.; Edwards, W.; Ragusa, J. V.; Wine, J. T.; Wong Gutierrez, D.; Airola, M. V.; Herring, L. E.; Coleman, R. A.; Klett, E. L.; Cohen, S. PLIN5 interacts with FATP4 at membrane contact sites to promote lipid droplet-to-mitochondria fatty acid transport. *Developmental Cell* **2023**, *58* (14), 1250-1265.e1256. DOI: https://doi.org/10.1016/j.devcel.2023.05.006.

(40) Benador, I. Y.; Veliova, M.; Mahdaviani, K.; Petcherski, A.; Wikstrom, J. D.; Assali, E. A.; Acin-Perez, R.; Shum, M.; Oliveira, M. F.; Cinti, S.; et al. Mitochondria Bound to Lipid Droplets Have Unique Bioenergetics, Composition, and Dynamics that Support Lipid Droplet Expansion. *Cell Metabolism* **2018**, *27* (4), 869-+. DOI: 10.1016/j.cmet.2018.03.003.

(41) Krahmer, N.; Najafi, B.; Schueder, F.; Quagliarini, F.; Steger, M.; Seitz, S.; Kasper, R.; Salinas, F.; Cox, J.; Uhlenhaut, N. H.; et al. Organellar Proteomics and Phospho-Proteomics Reveal Subcellular Reorganization in Diet-Induced Hepatic Steatosis. *Dev Cell* **2018**, *47* (2), 205-221 e207. DOI: 10.1016/j.devcel.2018.09.017 From NLM Medline.

(42) Reid, M. V.; Fredickson, G.; Mashek, D. G. Mechanisms coupling lipid droplets to MASLD pathophysiology. *Hepatology* **2024**, 10.1097/HEP.0000000000001141. DOI: 10.1097/hep.0000000000001141.

(43) Hardy, T.; Oakley, F.; Anstee, Q. M.; Day, C. P. Nonalcoholic Fatty Liver Disease: Pathogenesis and Disease Spectrum. *Annu Rev Pathol* **2016**, *11*, 451-496. DOI: 10.1146/annurev-pathol-012615-044224.

(44) Tan, Y.; Jin, Y.; Wang, Q.; Huang, J.; Wu, X.; Ren, Z. Perilipin 5 Protects against Cellular Oxidative Stress by Enhancing Mitochondrial Function in HepG2 Cells. *Cells* **2019**, *8* (10). DOI: 10.3390/cells8101241 From NLM Medline.

(45) Keenan, S. N.; Meex, R. C.; Lo, J. C. Y.; Ryan, A.; Nie, S.; Montgomery, M. K.; Watt, M. J. Perilipin 5 Deletion in Hepatocytes Remodels Lipid Metabolism and Causes Hepatic Insulin Resistance in Mice. *Diabetes* **2019**, *68* (3), 543-555. DOI: 10.2337/db18-0670.

(46) Mass-Sanchez, P. B.; Krizanac, M.; Stancl, P.; Leopold, M.; Engel, K. M.; Buhl, E. M.; van Helden, J.; Gassler, N.; Schiller, J.; Karlic, R.; et al. Perilipin 5 deletion protects against nonalcoholic fatty liver disease and hepatocellular carcinoma by modulating lipid metabolism and inflammatory responses. *Cell Death Discov* **2024**, *10* (1), 94. DOI: 10.1038/s41420-024-01860-4 From NLM PubMed-not-MEDLINE.

(47) Parlakgul, G.; Arruda, A. P.; Pang, S.; Cagampan, E.; Min, N.; Guney, E.; Lee, G. Y.; Inouye, K.; Hess, H. F.; Xu, C. S.; Hotamisligil, G. S. Regulation of liver subcellular architecture controls metabolic homeostasis. *Nature* **2022**, *603* (7902), 736-742. DOI: 10.1038/s41586-022-04488-5 From NLM Medline.

(48) Beaulant, A.; Dia, M.; Pillot, B.; Chauvin, M. A.; Ji-cao, J. W.; Durand, C.; Bendridi, N.; Chanon, S.; Vieille-Marchiset, A.; Da Silva, C. C.; et al. Endoplasmic reticulum-mitochondria miscommunication is an early and causal trigger of hepatic insulin resistance and steatosis. *Journal of Hepatology* **2022**, *77* (3), 710-722. DOI: 10.1016/j.jhep.2022.03.017.

(49) Casellas-Díaz, S.; Larramona-Arcas, R.; Riqué-Pujol, G.; Tena-Morraja, P.; Müller-Sánchez, C.; Segarra-Mondejar, M.; Gavaldà-Navarro, A.; Villarroya, F.; Reina, M.; Martínez-Estrada, O. M.; Soriano, F. X. Mfn2 localization in the ER is necessary for its bioenergetic function and neuritic development. *Embo Reports* **2021**, *22* (9). DOI: ARTN e51954 10.15252/embr.202051954.

(50) Freyre, C. A. C.; Rauher, P. C.; Ejsing, C. S.; Klemm, R. W. MIGA2 Links Mitochondria, the ER, and Lipid Droplets and Promotes Lipogenesis in Adipocytes. *Molecular Cell* **2019**, *76* (5), 811-+. DOI: 10.1016/j.molcel.2019.09.011.

(51) Valm, A. M.; Cohen, S.; Legant, W. R.; Melunis, J.; Hershberg, U.; Wait, E.; Cohen, A. R.; Davidson, M. W.; Betzig, E.; Lippincott-Schwartz, J. Applying systems-level spectral imaging and analysis to reveal the organelle interactome. *Nature* **2017**, *546* (7656), 162-167. DOI: 10.1038/nature22369.

(52) Rhoads, S. N.; Dong, W.; Hsu, C.-H.; Mfulama, N. R.; Yarlagadda, R.; Ragusa, J. V.; Ye, M.; Henrie, A.; Zanellati, M. C.; Diering, G. H.; et al. Neurons and astrocytes have distinct organelle signatures and responses to stress. *Cell Reports* **2025**, *44* (9), 116280. DOI: https://doi.org/10.1016/j.celrep.2025.116280.

(53) Porat-Shliom, N.; Harding, O. J.; Malec, L.; Narayan, K.; Weigert, R. Mitochondrial Populations Exhibit Differential Dynamic Responses to Increased Energy Demand during Exocytosis In Vivo. *iScience* **2019**, *11*, 440-449. DOI: 10.1016/j.isci.2018.12.036.

(54) Cunningham, R. P.; Kang, S. W. S.; Porat-Shliom, N. Location matters: Cellular heterogeneity in the hepatic lobule and hepatocellular carcinoma. *Am J Physiol Gastrointest Liver Physiol* **2023**. DOI: 10.1152/ajpgi.00278.2022 From NLM Publisher.

(55) van der Walt, S.; Schönberger, J. L.; Nunez-Iglesias, J.; Boulogne, F.; Warner, J. D.; Yager, N.; Gouillart, E.; Yu, T. scikit-image: image processing in Python. *PeerJ* **2014**, *2*, e453. DOI: 10.7717/peerj.453 From NLM.

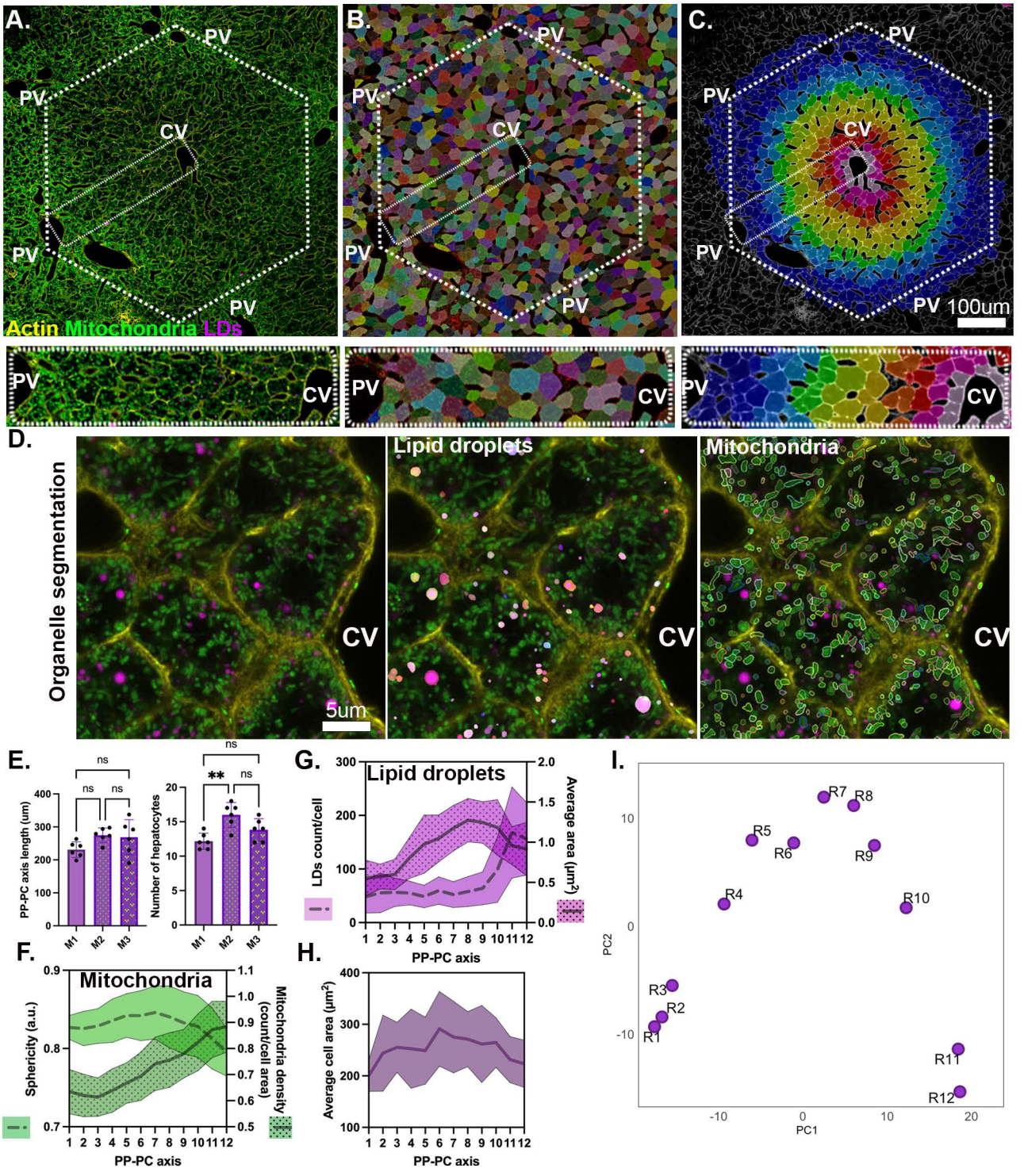

Figure 1. LD and mitochondiral topology define zones in the lobule

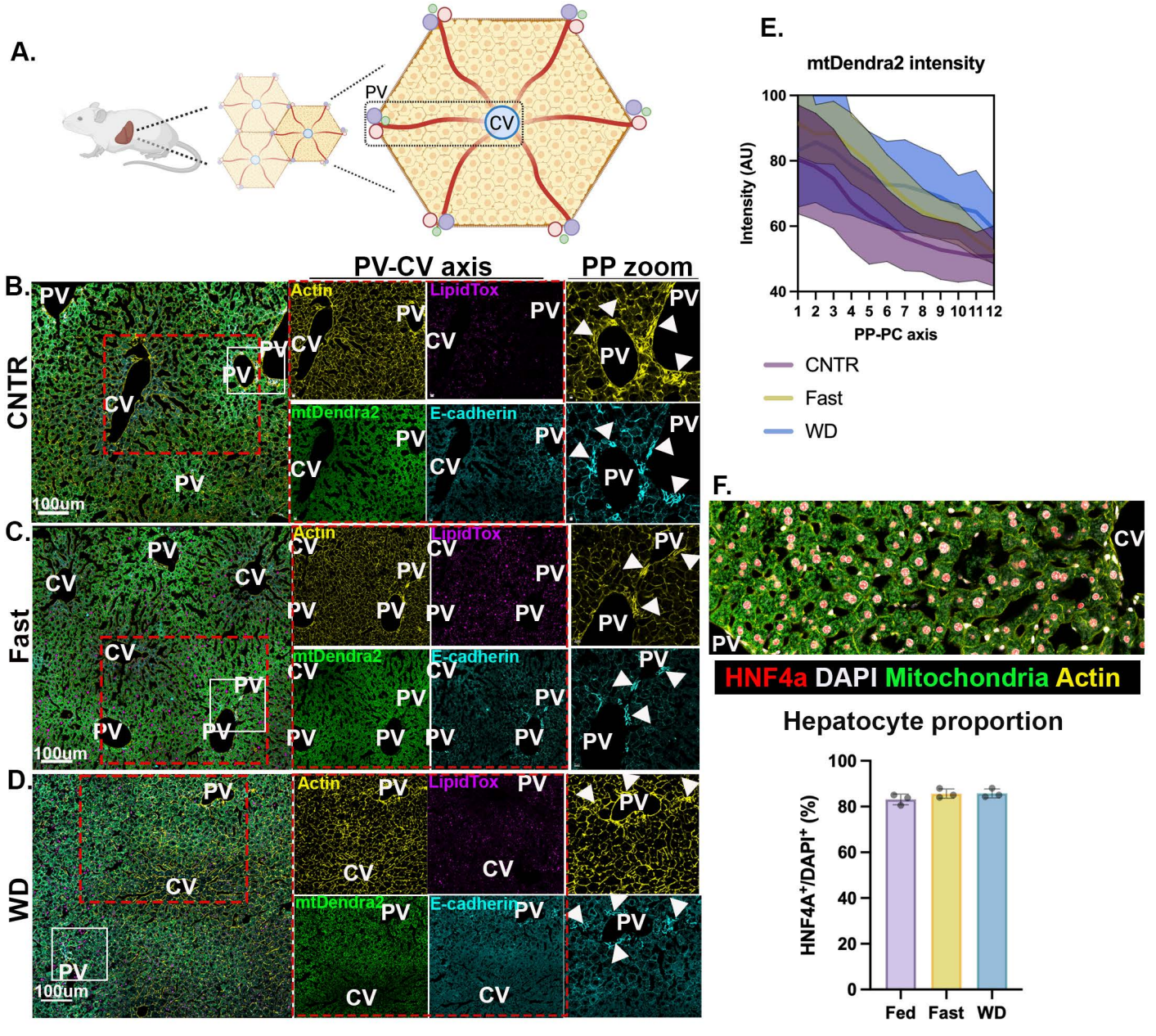

Extended Figure 1 Anatomical landmarks guide tissue orientation in scPhenomics

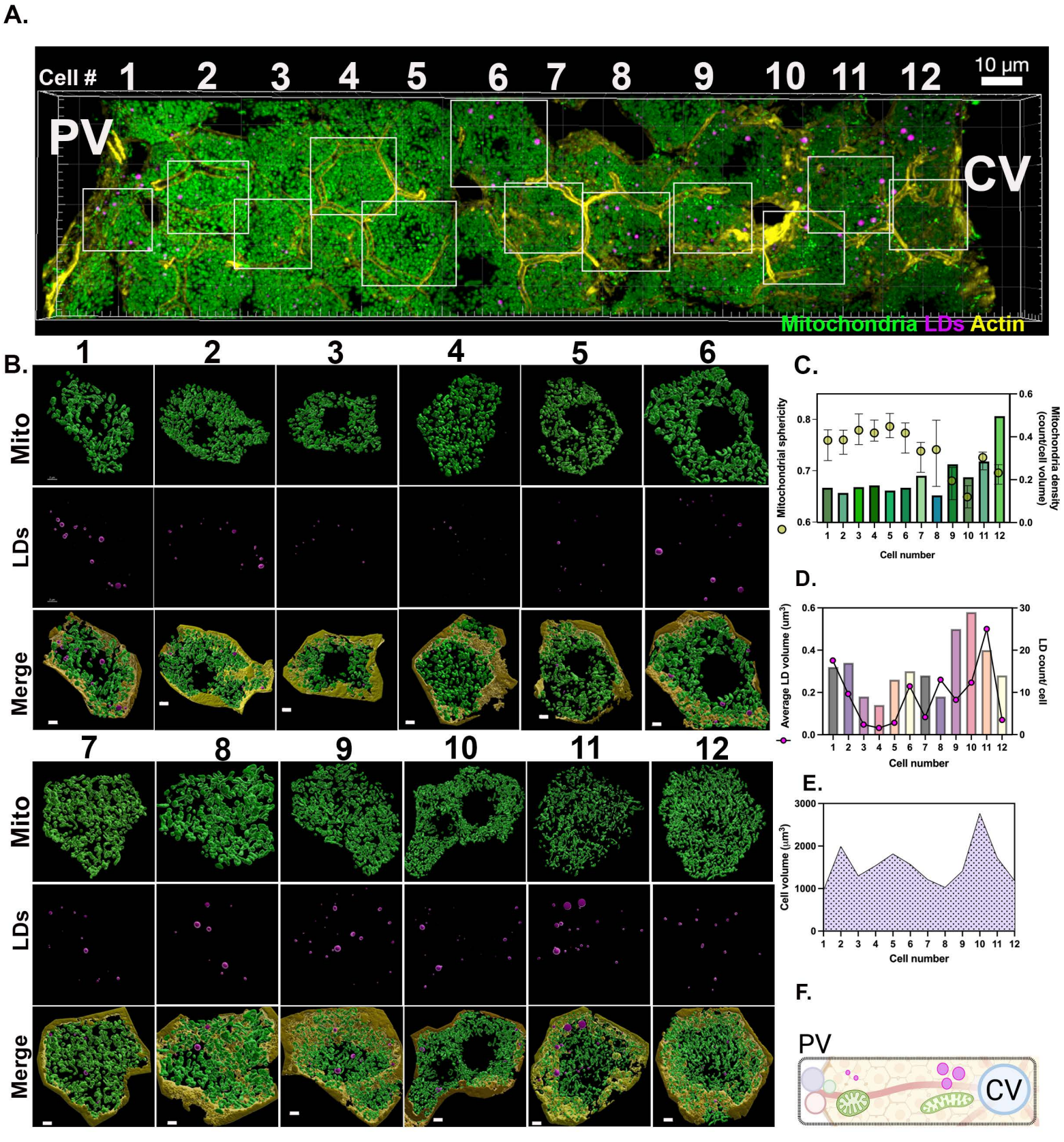

Extended Figure 2. Single-cell analysis of LD and mitochondrial structure in 3D

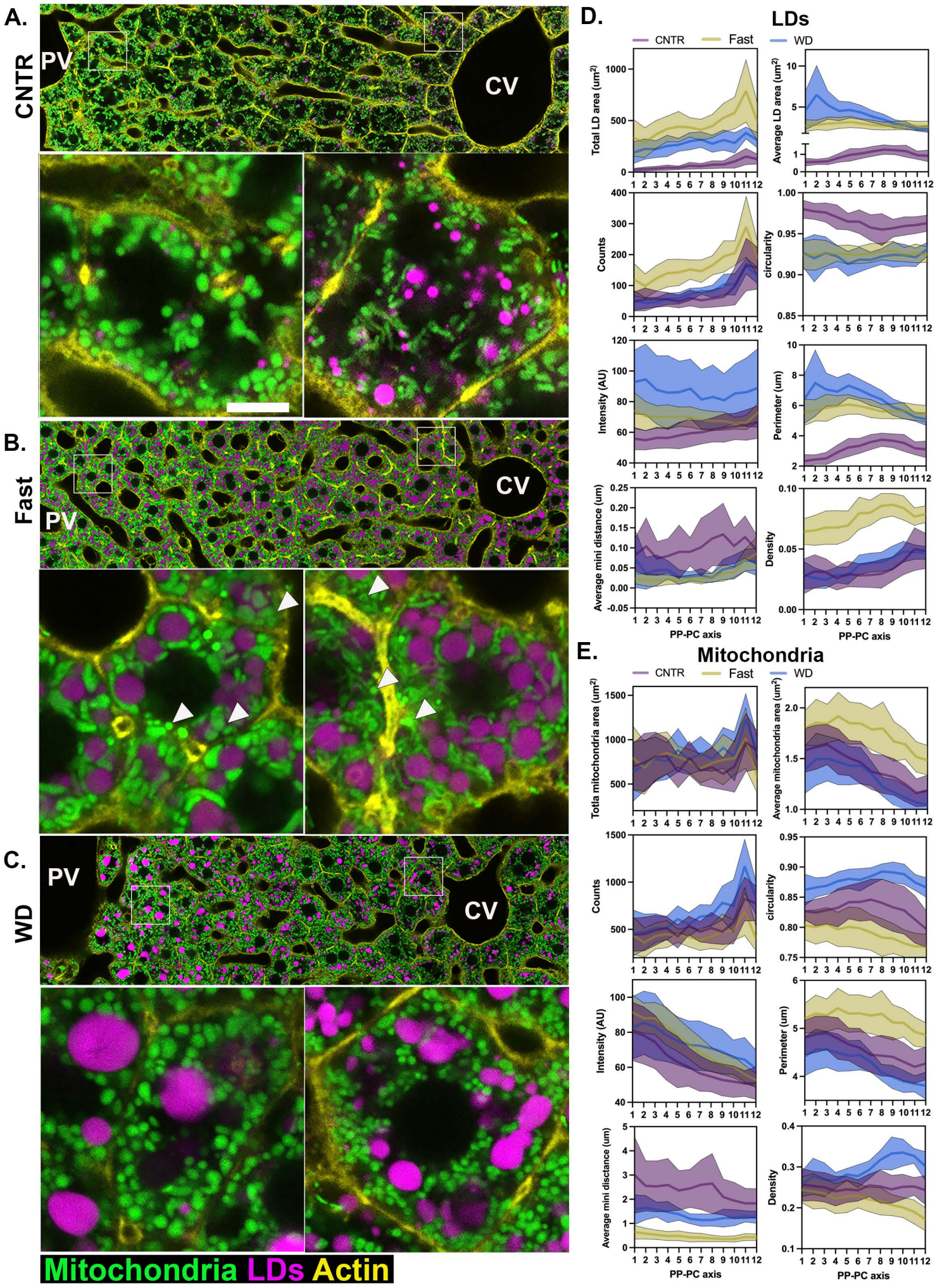

Fig. 2 Increased lipid flux induces rewiring of LD and mitochondria circuits

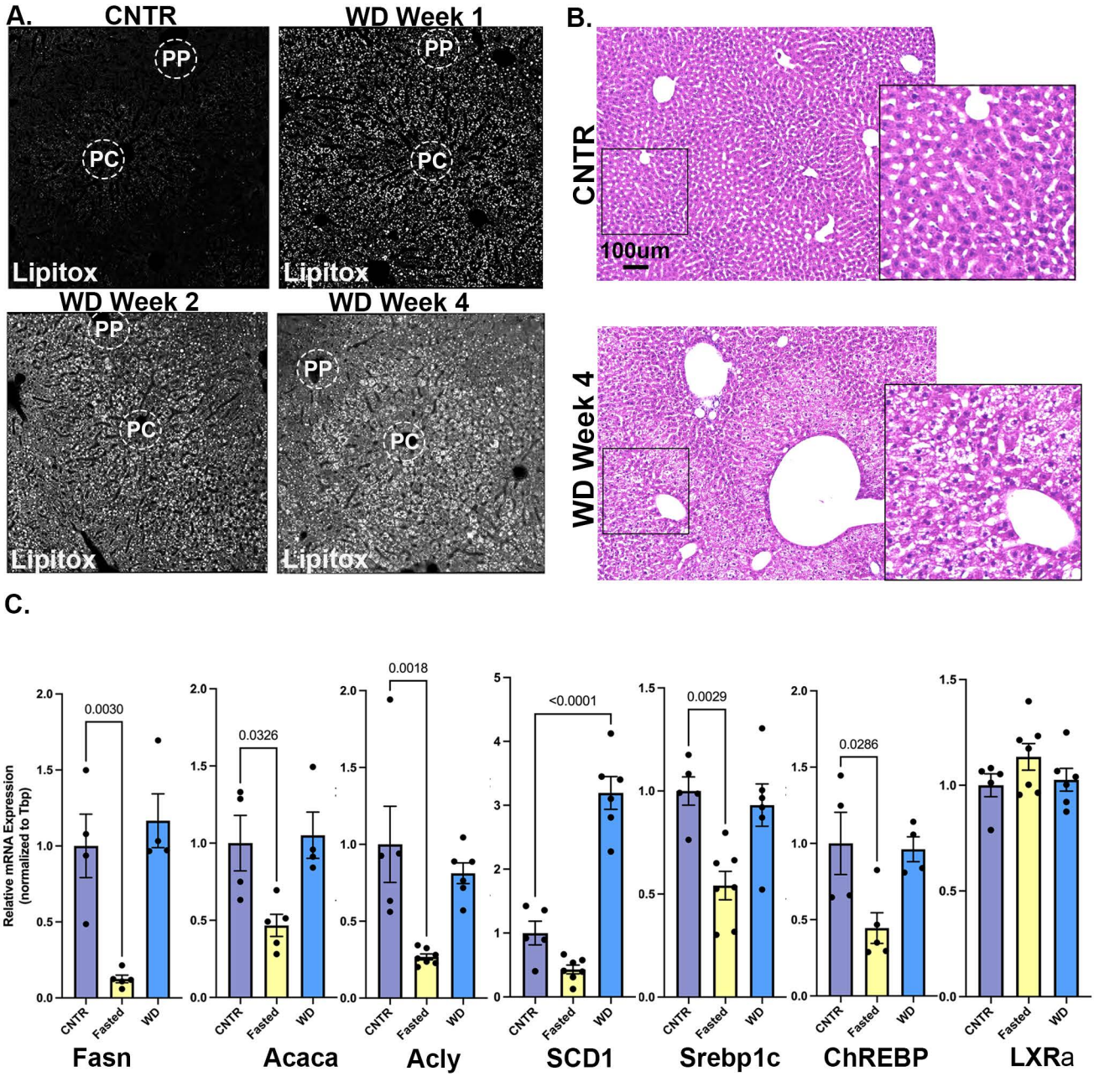

Extended Figure 3. Hepatic steatosis and DNL in short-term WD feeding

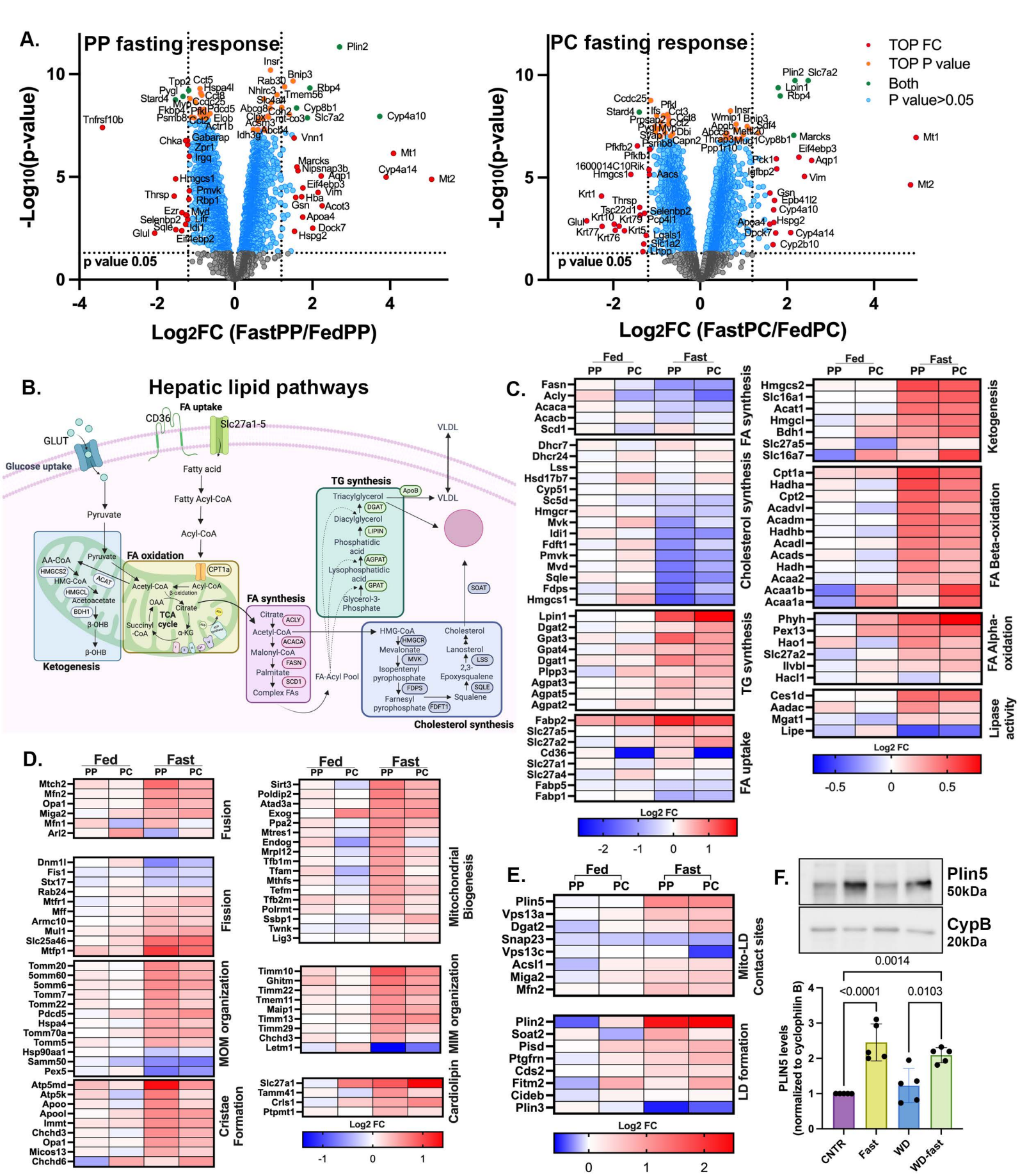

Fig 4. Fasting-induced remodeing of hepatic proteome

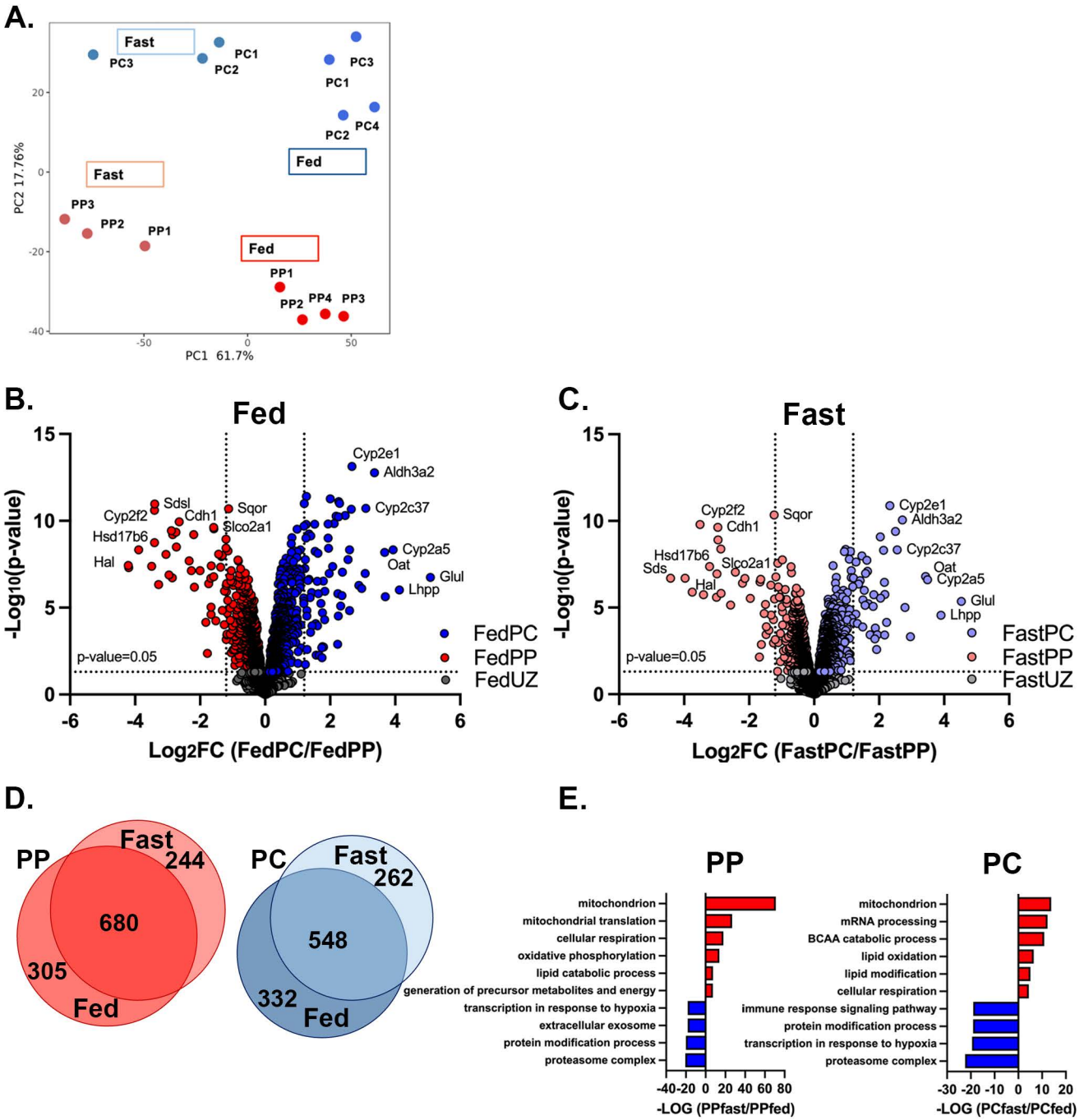

Extended Figure 4. Comparative proteomics of spatially sorted hepatocytes

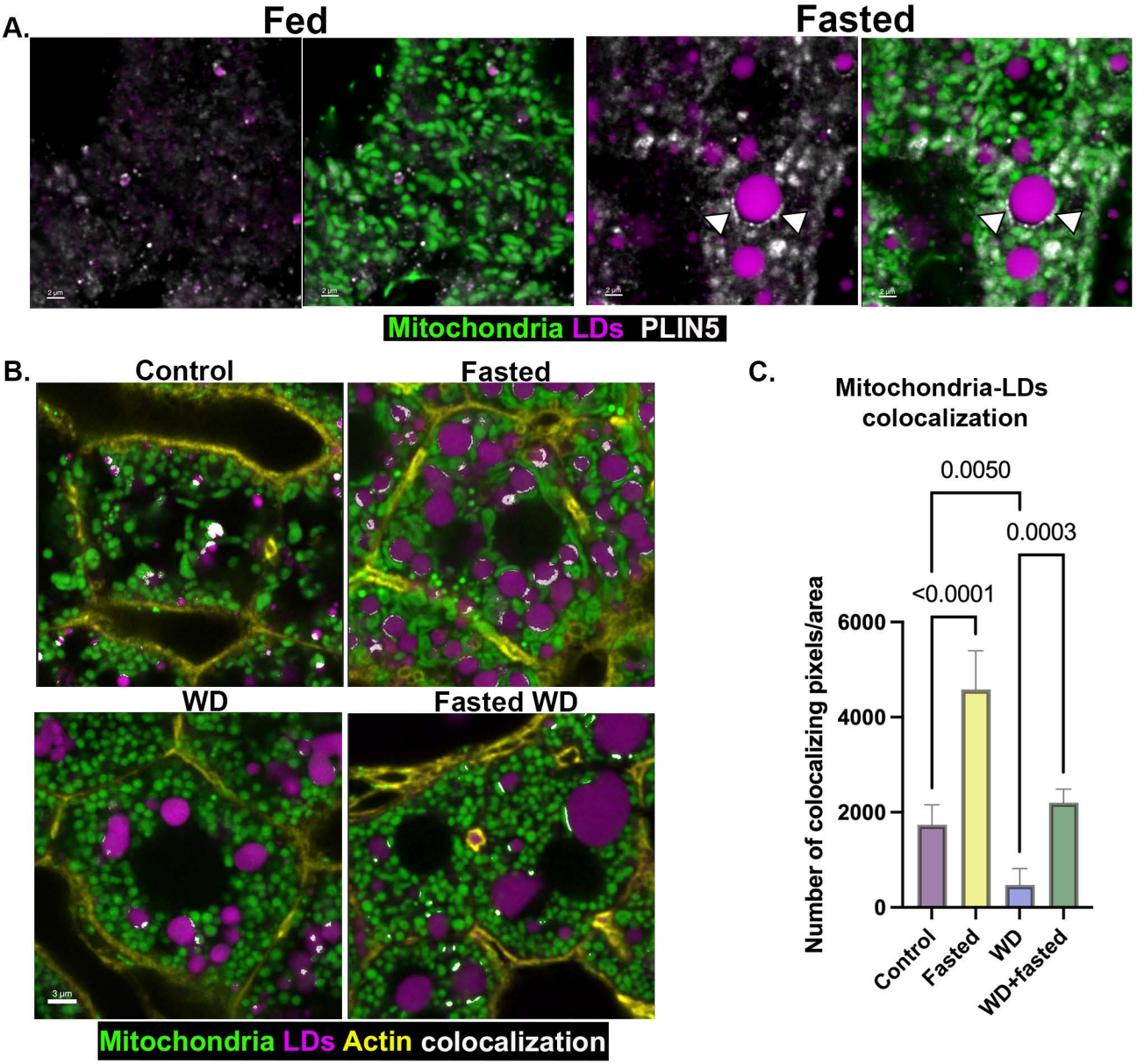

Extended Figure 5. Fasting induce Mitochondria-LD interactions

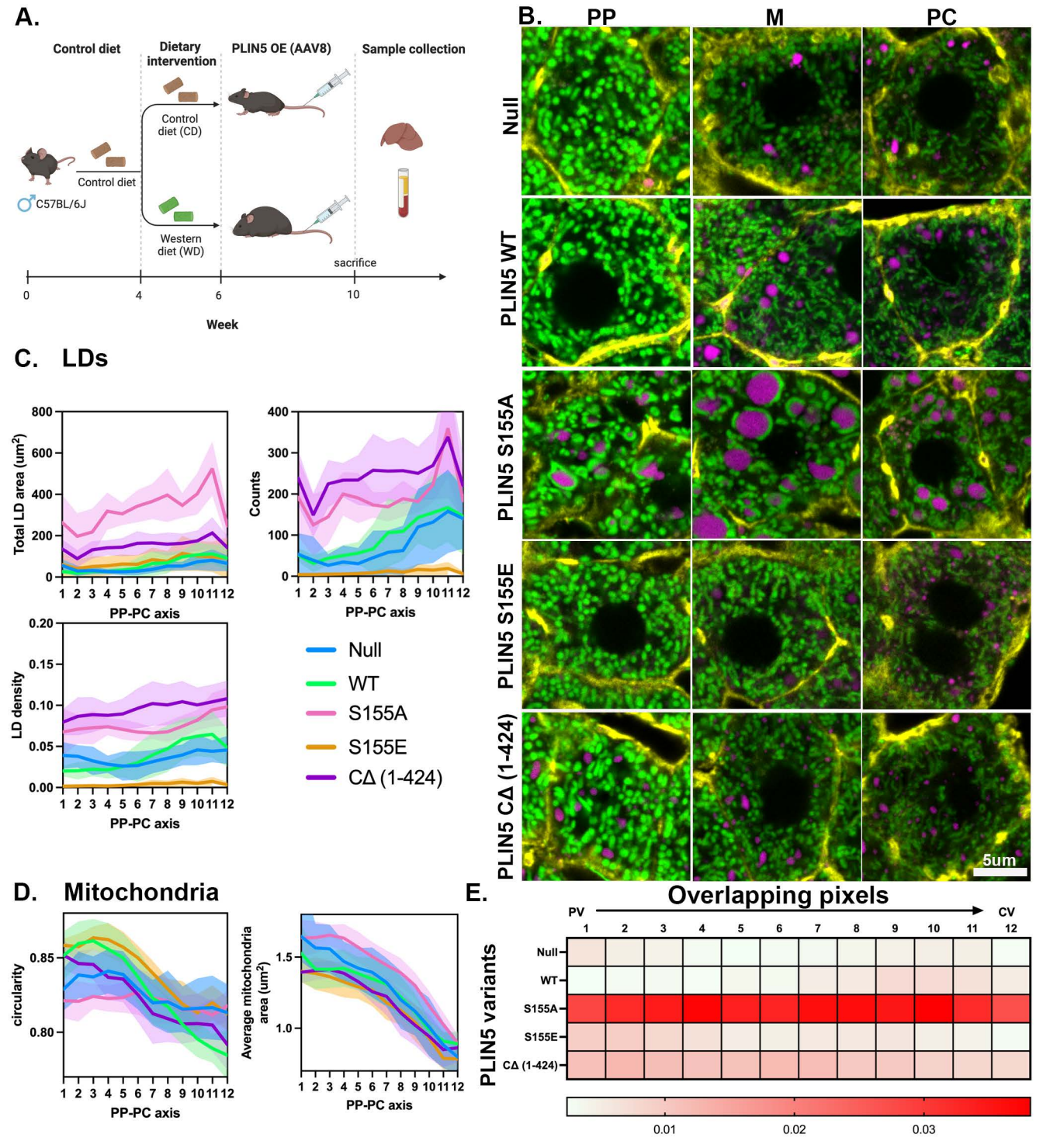

Fig 5. Mitochondria-LD contacts promote LD expansion in vivo

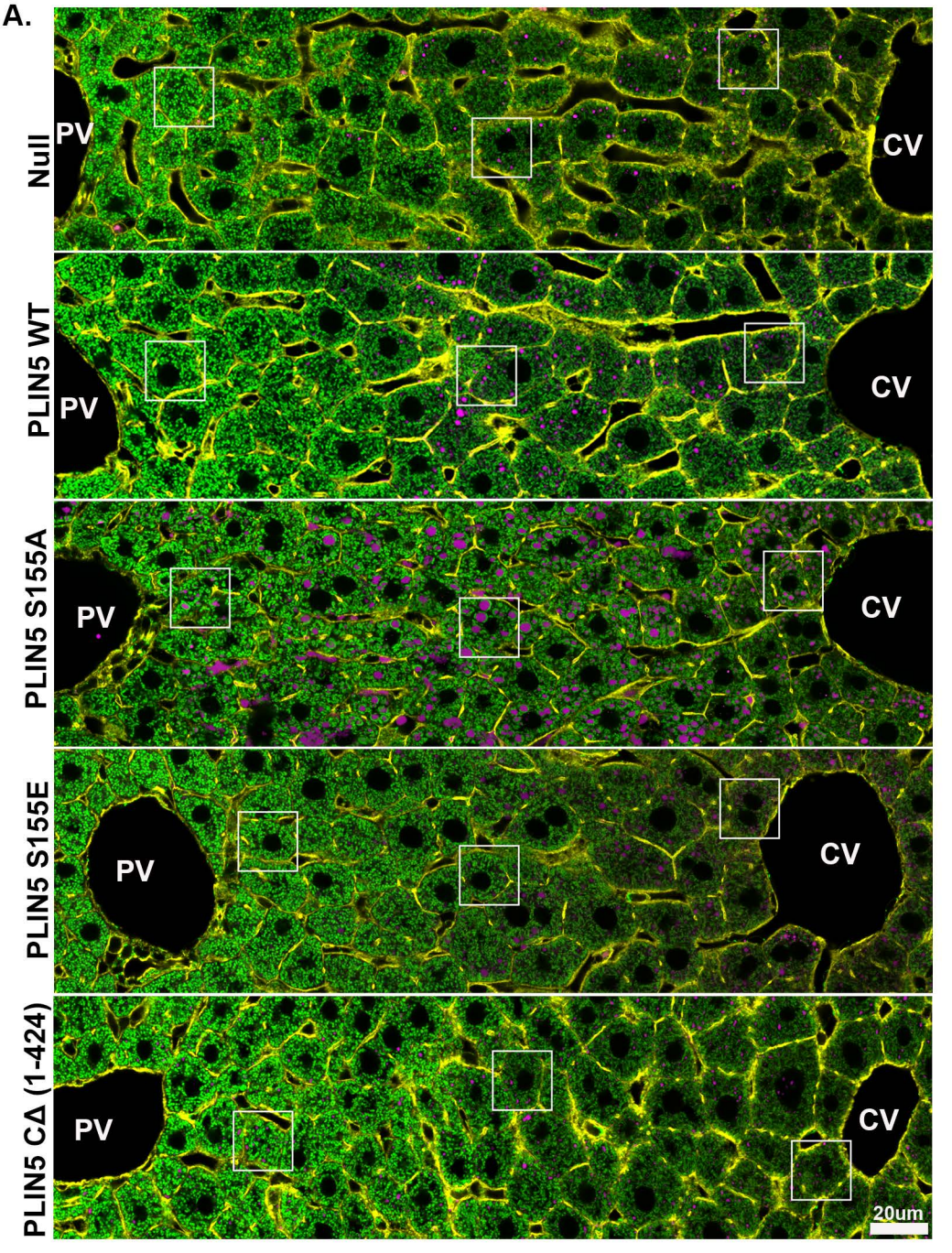

Extended Figure 6. In vivo remodeling of mitochondria-LDs interactions

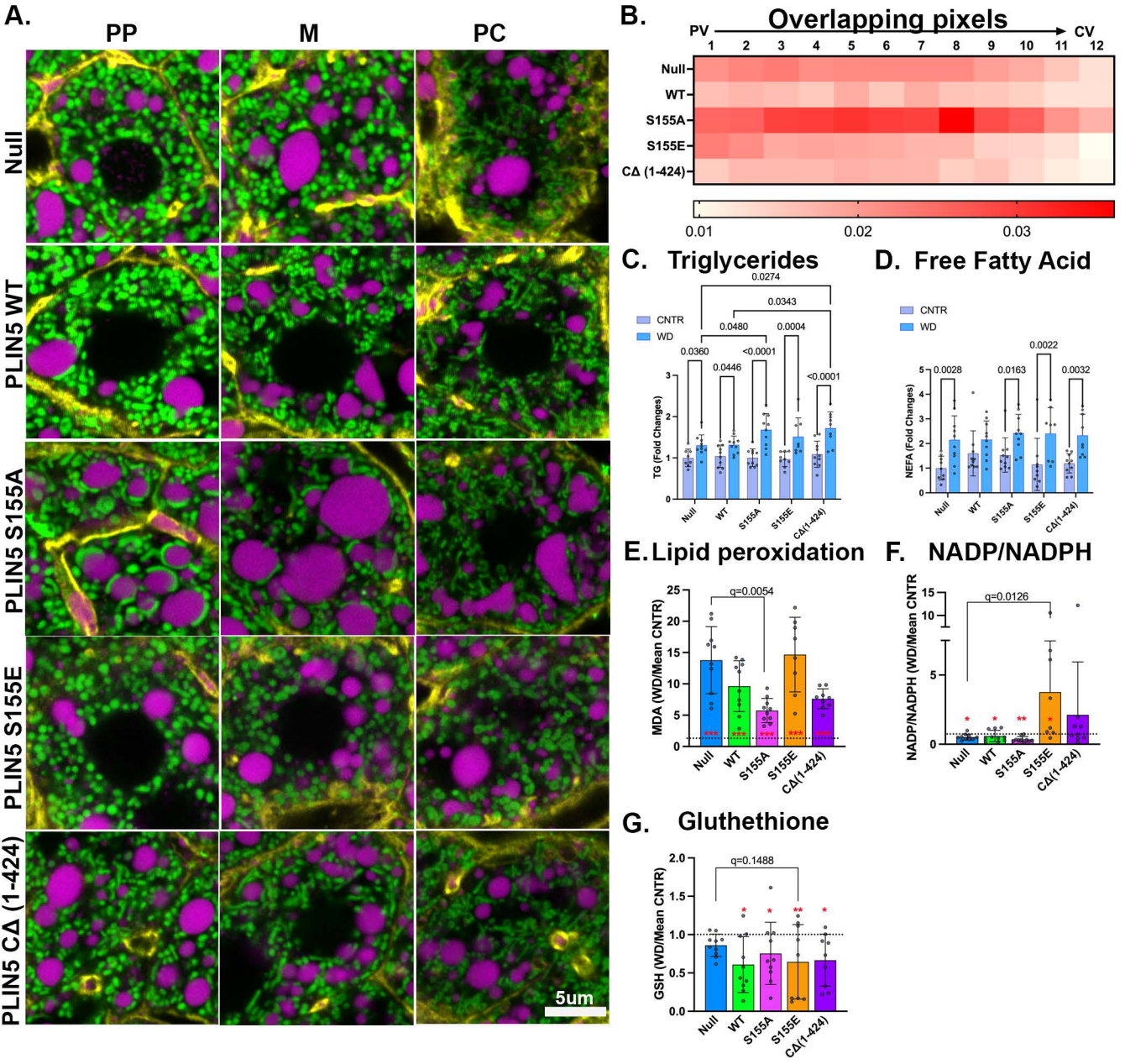

Fig. 6
Mitochondria-LD contacts promote lipid storage, reducing WD-induced lipotoxicity

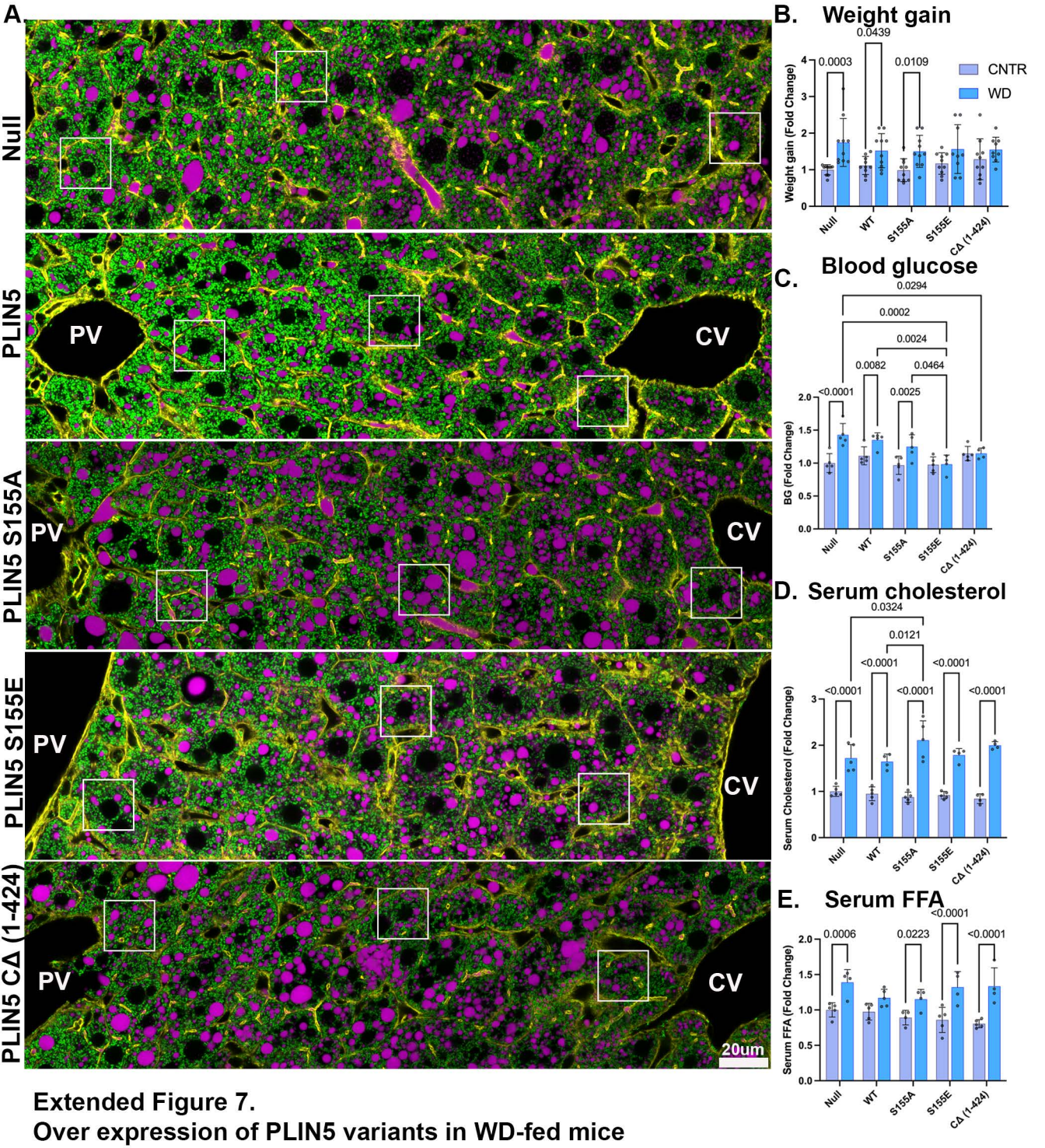

Extended Figure 7.
Over expression of PLIN5 variants in WD-fed mice

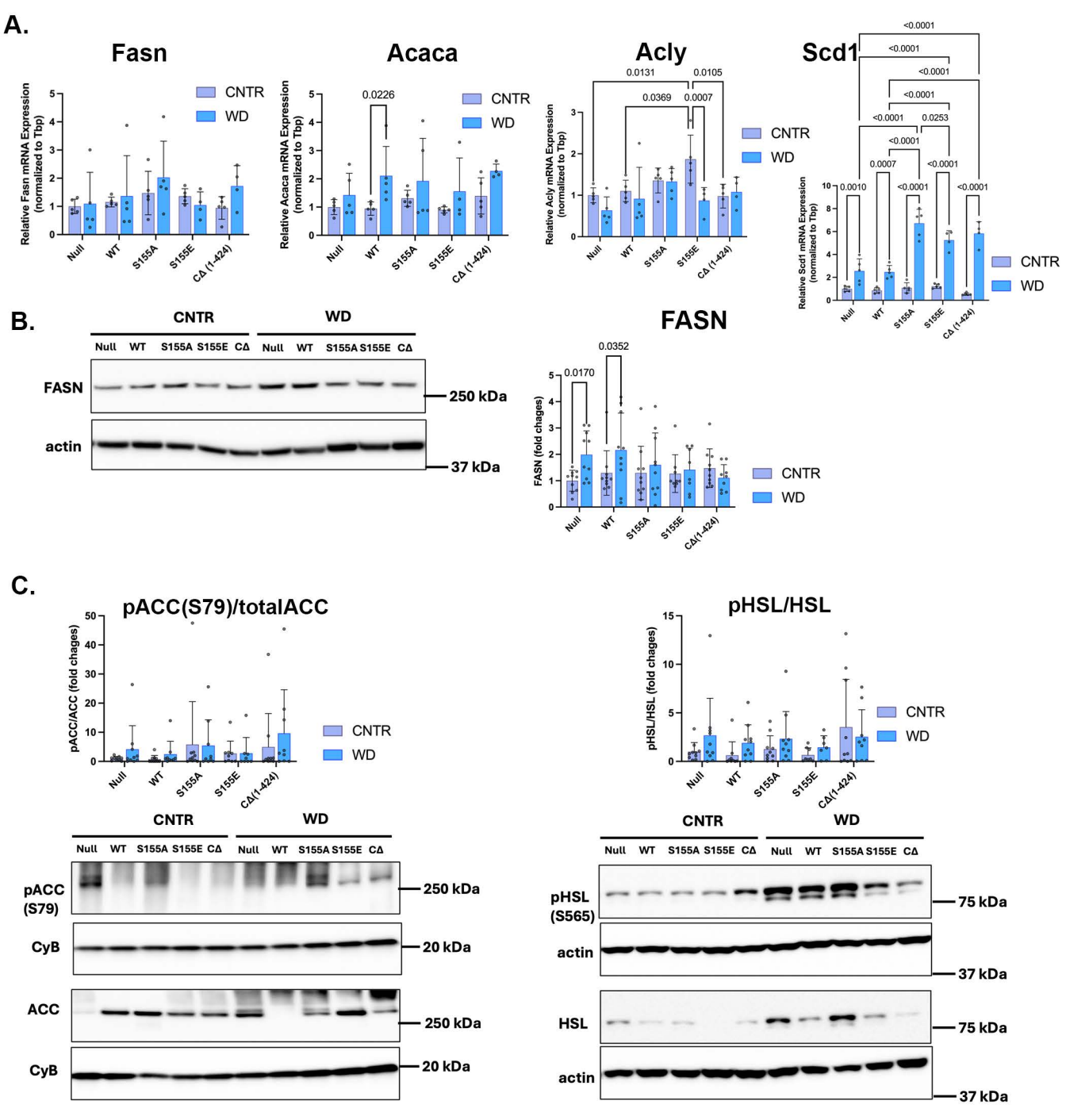

Extended Figure 8. The effect of PLIN5 variants and WD on DNL

A.

#	Steatosis	Inflammation	Fibrosis
1	Minimal	None	None
2	None	None	None
3	None	None	None
4	Mild	Minimal	None
5	None	Mild	None
6	None	None	None
7	None	Minimal	None
8	Mild	Minimal	None
9	Minimal	Minimal	None
10	Mild	Mild	None
11	None	Mild	None
12	None	None	None

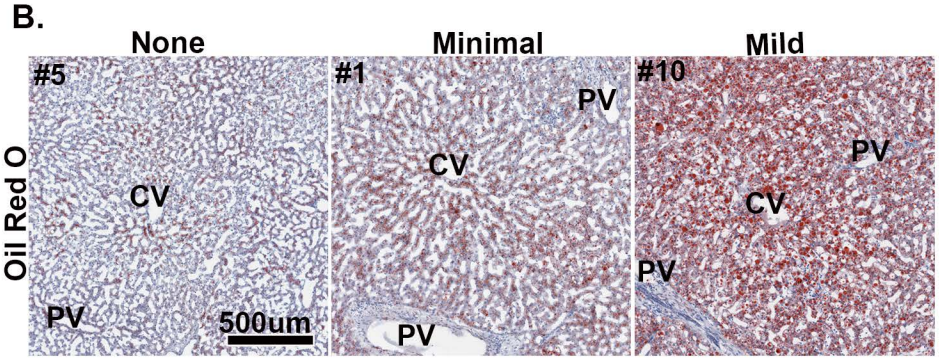

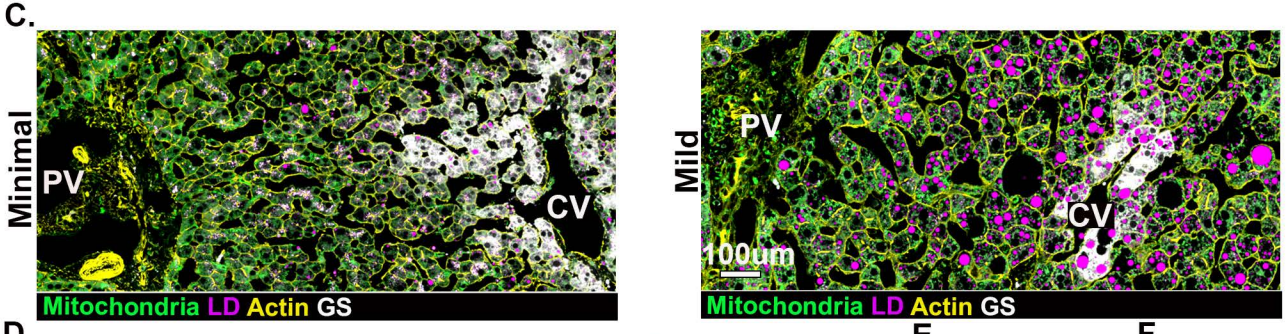

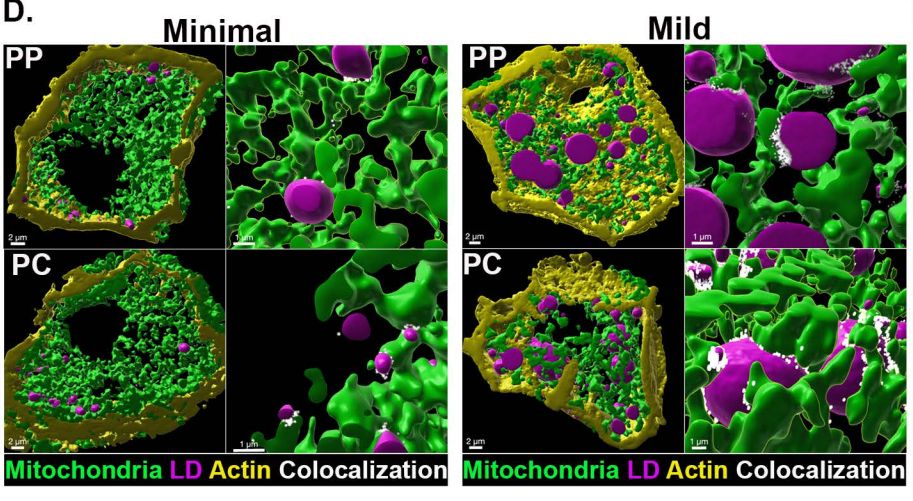

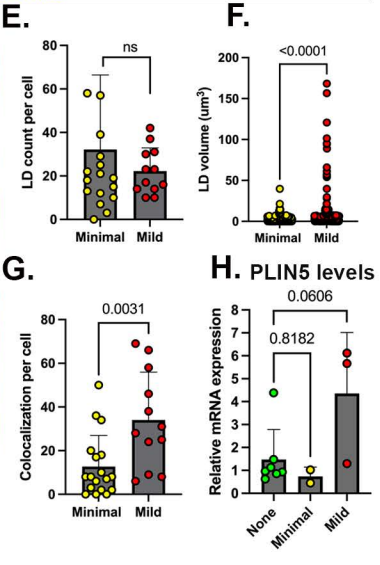

Figure 7.
Mitochondria-LD contacts are associated with higher lipid content in human livers

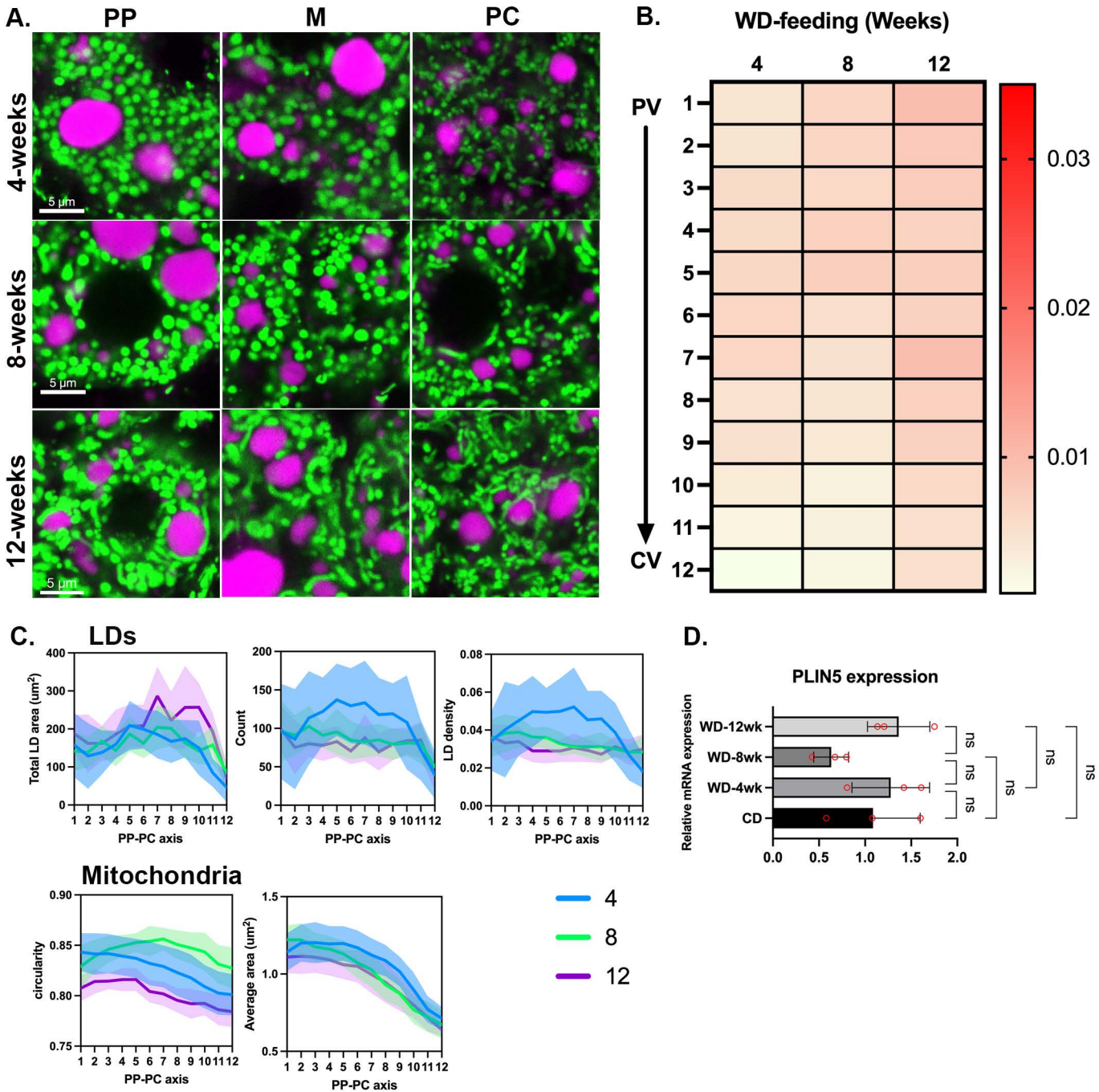

Extended Figure 9.
Increased mitochondria-LD interactions correlate with prolonged WD-feeding in mice.

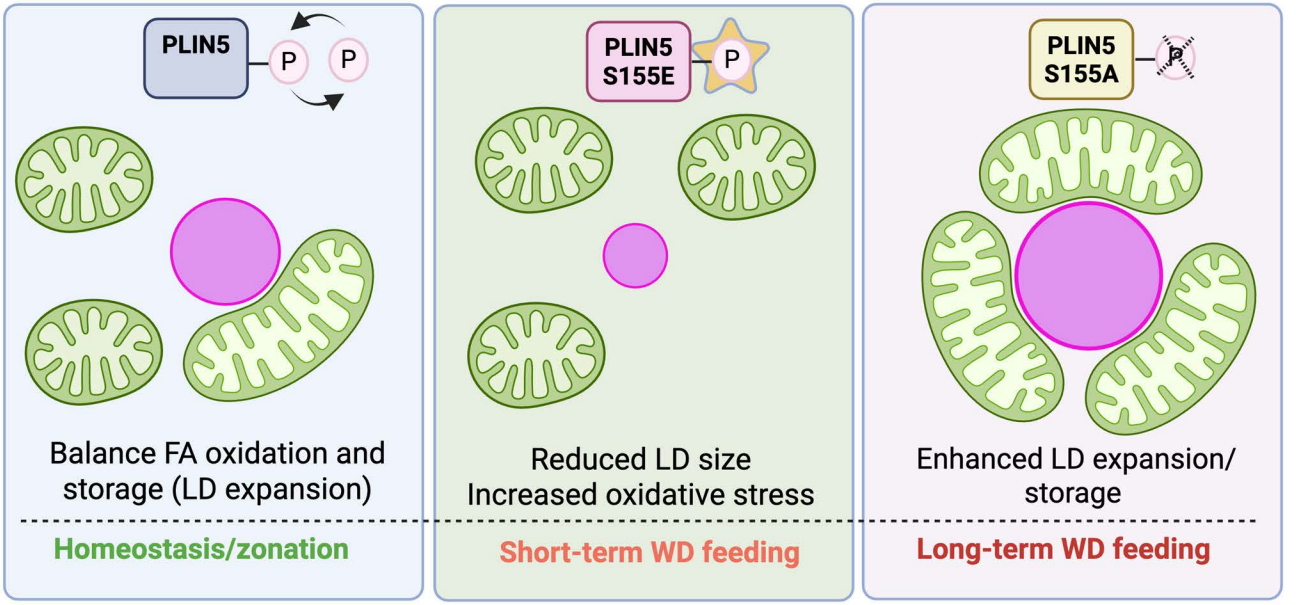

FA: Fatty Acid; PLIN5: Perilipin 5; LD: lipid droplet; WD: western diet

Figure 8. PLIN5-induced mitochondria-LD contacts regulate lipid homeostasis

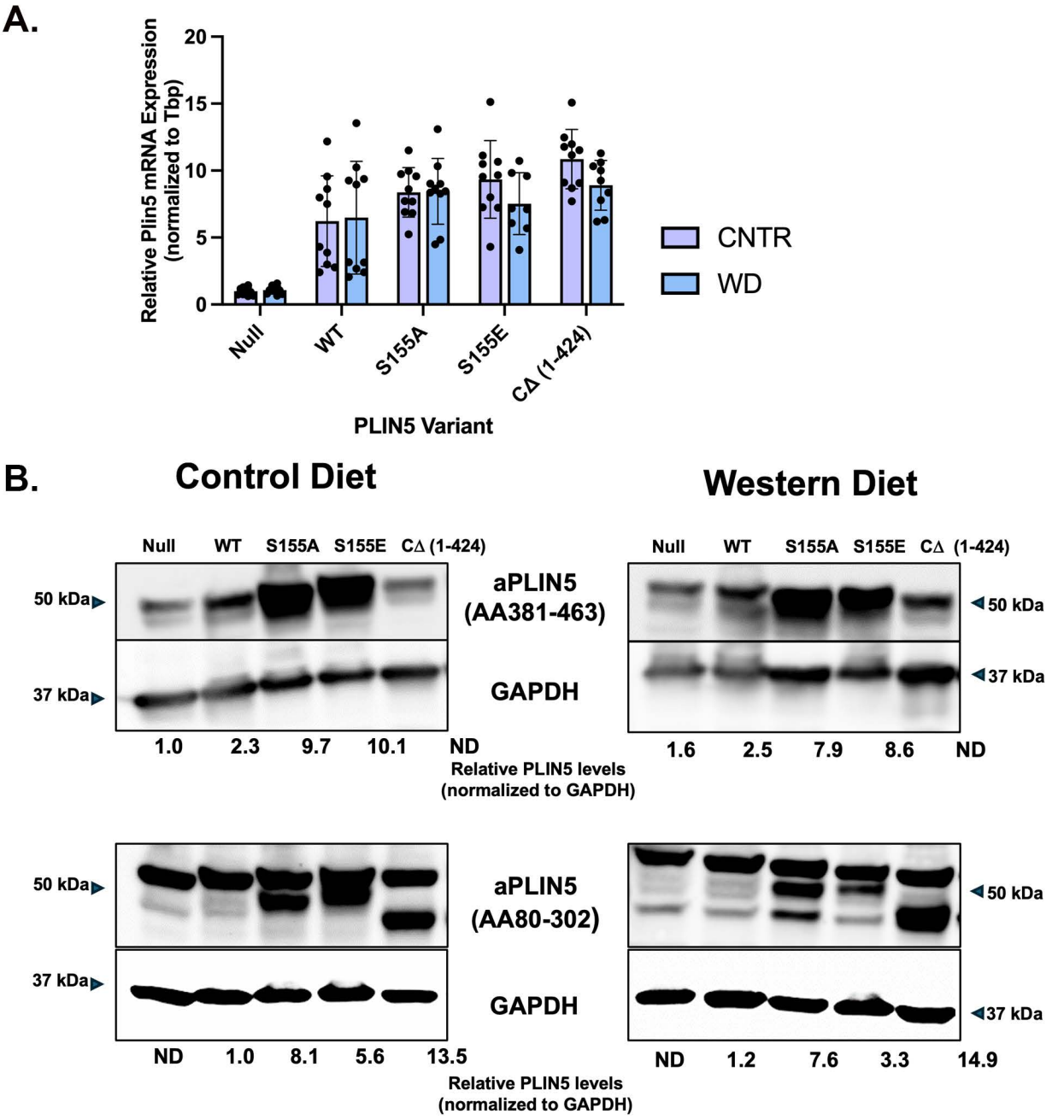

Supplementary Figure 1. In vivo overexpression of PLIN5